Department of Physics and Astronomy

University of Heidelberg

Diploma thesis

in Physics

submitted by

Johanna Elise Bohn

born in Konstanz

2012

Towards an ultracold three-component Fermi Gas
in a two-dimensional optical lattice

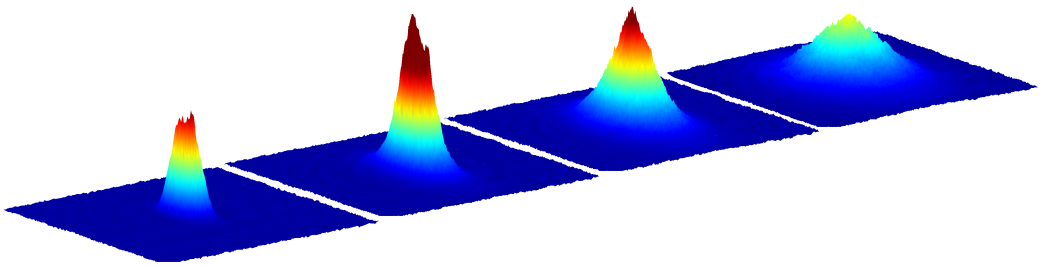

This diploma thesis has been carried out by

Johanna Elise Bohn

at the Physikalisches Institut Heidelberg

and the Max-Planck-Institut für Kernphysik

under the supervision of

Professor Dr. Selim Jochim

Abstract

This thesis reports on the progress towards the preparation of an ultracold three-component Fermi gas of ^{6}Li in a two-dimensional optical lattice.
An optical dipole trap was set up and filled with ultracold atoms from a magneto-optical trap, which were then evaporatively cooled. In a trap with an average trap frequency of 146 Hz at an aspect ratio of 1:9:42 a degenerate, non-interacting Fermi gas of 150 000 atoms was created with a lifetime of 42 s. In the same trap a molecular Bose-Einstein condensate of approximately 25 000 $^6Li_2$ dimers was achieved.
Radio frequency pulses were applied to a two-component thermal gas to populate the third component and determine the maximum achievable Rabi frequency with this setup.
In the next step we want to transfer the evaporatively cooled cloud from the dipole trap into a two-dimensional potential. As this will be created by an interference pattern of two intersecting laser beams, tests were performed concerning the short- and long-term stability of the optical setup. On the basis of these measurements a compact and stable interferometer casing was designed and will be integrated into the experiment very soon.

Abstract

Diese Arbeit beschreibt den Fortschritt zur Herstellung eines ultrakalten drei-komponentigen Fermi-Gases aus ^{6}Li in einem zweidimensionalen optischen Gitter.
Eine optische Dipolfalle wurde aufgebaut und mit ultrakalten Atomen aus einer magneto-optischen Falle gefüllt. In einer Falle mit einer mittleren Fallenfrequenz von 146 Hz bei einem Aspekt-Verhältnis von 1:9:42 wurde durch evaporatives Kühlen ein entartetes, nicht wechselwirkendes Fermi Gas aus 150 000 Atomen mit einer Lebensdauer von 42 s hergestellt. In derselben Falle wurde ein molekulares Bose-Einstein Kondensat aus etwa 25 000 $^6Li_2$ Dimeren erreicht.
Radiofrequenz-Pulse wurden in ein zwei-komponentiges thermisches Gas eingestrahlt, um die dritte Komponente zu bevölkern und die mit diesem Aufbau maximal erreichbare Rabi-Frequenz zu bestimmen.
Im nächsten Schritt soll das evaporativ gekühlte Gas aus der Dipolfalle in ein zweidimensionales Potential transferiert werden. Da dieses aus dem Interferenzmuster zweier sich kreuzender Laserstrahlen ensteht, wurden die Kurz- und Langzeitstabilität des optischen Aufbaus getestet. Auf Grundlage dieser Messungen wurde ein kompaktes und stabiles Interferometer-Gehäuse entwickelt, das in naher Zukunft in den Experiment-Aufbau integriert wird.

Contents

1 Introduction

One of the most active areas of research in ultracold quantum gases today is the preparation and study of strongly correlated systems, trying to observe exotic phenomena such as polarons, the Tonks-Girardeau state or d-wave superfluidity. Ironically, what made ultracold quantum gases so successful in the first place was the possibility to study fundamental quantum mechanical effects in dilute and weakly interacting systems.

This enabled a better understanding of the detailed properties of quantum degenerate systems, which had long been the subject of extensive research since they play an important role in such diverse fields as condensed matter, atomic, nuclear and astrophysics. In the past this proved difficult as the particles in such systems are generally quite densely packed and are thus in many cases strongly interacting, which makes theoretical descriptions very difficult. Earlier approaches to circumvent this problem studied Bose-Einstein condensation in excitonic systems where interactions are weak [Lin93]. However, they were only poorly understood and difficult to probe. Then, in 1995 three independent research groups were successful in preparing a dilute atomic gas exhibiting one of the most striking quantum mechanical phenomena, the phase transition of a Bose gas into a Bose-Einstein condensate. This had been predicted by Satyendra Nath Bose and Albert Einstein in 1925 [Ein25, And95, Bra95, Dav95]. What set this new approach apart was that by cooling the gas to very low temperatures quantum degeneracy could be reached although the gas was very dilute and thus only weakly interacting.

In the following years ultracold Bose and Fermi gases were found to be ideally suited to understand quantum phenomena from first principles, and thus facilitating the understanding of more complex, strongly interacting quantum systems. Important milestones were the first observation of a degenerate Fermi gas [DeM99], the preparation of a molecular Bose-Einstein condensate [Joc03, Gre03, Zwi03] and measurements across the BEC-/BCS crossover [Bar04]. Key advantages of ultracold atomic

gases were their easy accessibility by optical imaging and their great tunability: By preparing the system in optical traps magnetic fields could be used to tune the interparticle interactions across a Feshbach resonance [Ino98].
In recent years ultracold Fermi gases have gained substantial interest as model systems with unequaled controllability promising insight into many fundamental effects known from other branches of physics as well as completely new phenomena. For instance they are used in the simulation of solid-state systems [Hof02, Ess10]: Two-component Fermi gases can exhibit the same fundamental physics as a solid without being influenced by the environment or hindered by unwanted perturbations like defects and impurities in the atomic lattice. Fermionic atoms in two hyperfine states represent the electrons in their two possible states, spin up and spin down. The key link between the two systems are optical lattices, providing an environment for the atoms equivalent to that of a crystal lattice for electrons.
But ultracold Fermi gases are not just limited to the study of solid-state effects. Simply by adding atoms in a third state ultracold Fermi gases can also provide experimental access to a wealth of completely different phenomena. With a three-component Fermi gas a system with approximate $SU(3)$ symmetry can be created, with which questions related to high-energy physics such as color superfluidity or baryon formation from quarks can be studied [Rap07, Wil07]. The atomic species we use in our experiments, ^{6}Li, is uniquely suited for this, as the interactions between the three states can all be made resonant at the same time.
Our group was the first to study three-component Fermi gases of ^{6}Li atoms in the three lowest hyperfine substates [Ott08]. In this system experimental evidence of a universal trimer state predicted by Vitaly Efimov in 1970, the Efimov trimer [Wen09], was found. Its binding energy could be measured for the first time using radio frequency spectroscopy [Lom10]. However, three-component Fermi gases are subject to three-body loss rates which make the system unstable as soon as interactions become too strong. Thus studying a degenerate three-component Fermi gas with resonant interactions has so far been unattainable.
This impediment can be overcome by providing a periodic lattice potential for the atoms. In an optical lattice a quantum-Zeno effect is predicted to suppress tunneling and with it three-body loss [Kan09]. In order to prepare such a lattice system for two- and three-component Fermi gases of ultracold ^{6}Li we decided to build an entirely new

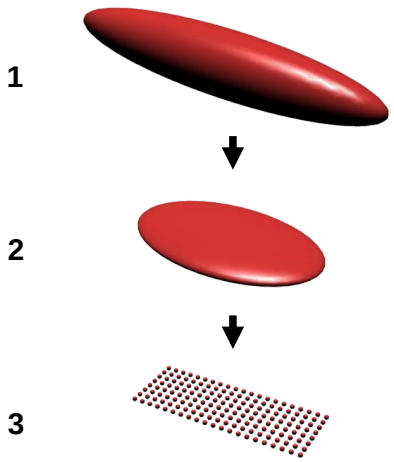

Figure 1.1: Milestones in the realization of a two-dimensional optical lattice system for ^{6}Li. First we will cool the atoms in an optical dipole trap (1) from where we will transfer them into a two-dimensional pancake shaped trap (2). This is then overlapped with an optical lattice creating a two-dimensional plane of lattice sites (3).

experimental apparatus based on the design which had already proven so successful in the first experimental setup. We decided to make the lattice two-dimensional since this enables a direct observation of the sample.
To this end we will load an optical dipole trap with atoms from a magneto-optical trap and evaporatively cool them. In the next step we will load the cold atomic cloud into a pancake shaped dipole trap creating a homogeneous two-dimensional system. In the last step we will superpose this with an optical lattice. The combination of the two-dimensional trap and the optical lattice provides us with a two-dimensional plane of lattice sites which the atoms can occupy. Figure 1.1 illustrates these three milestones on the way towards a three-component Fermi gas in a two-dimensional optical lattice.

In this thesis I will present the progress that has been made in the last year in this project. First I will give a brief theoretical introduction presenting the key features of degenerate Bose and Fermi gases in Chapter 2 concluding with a summary of the properties of ^{6}Li important for our experiments. In Chapter 3 I will discuss optical dipole traps as our main tool for trapping atoms and present the considerations which went into the design of the dipole traps in our experiment.
After that the experimental setup will be explained in detail, concentrating on those

components which were designed or built in the course of this thesis (Chapter 4). Starting from an atomic cloud in a magneto-optical trap we have built an optical dipole trap, transfered the atoms into it and evaporatively cooled them down to the Nanokelvin range. Working towards a two-dimensional trapping potential we have developed and thoroughly tested a new interferometer setup to produce the pancake shaped trap which will be installed in the experiment very soon.
With the newly built dipole trap we have produced a molecular Bose-Einstein condensate of $^6Li_2$ and have used radio frequency spectroscopy to populate different of the three lowest hyperfine states of ^{6}Li, laying the basis for the preparation of a three-component Fermi gas. The observation of the molecular BEC will be presented in Chapter 5 while the results of the radio frequency spectroscopy are discussed in Chapter 6.
In the last chapter (Chapter 7) I summarize the results of this thesis and give an outlook on the next steps to follow in the completion of the experimental apparatus as well as the goals of the project and what fascinating and exciting phenomena we intend to study with it.

2 Ultracold quantum gases

Contents

In this chapter we give a brief overview of the physics of ultracold Fermi and Bose gases based on the more detailed discussions in [Ket99, Ket08, Chi10, Gio08, Dal98]. First we discuss the key properties of ideal, non-interacting Bose and Fermi gases before turning to the scattering properties of interacting systems and introducing the concept of Feshbach resonances. Finally we discuss some of the properties of ^{6}Li which are important for the work presented in this thesis.

2.1 Non-interacting quantum gases

All particles in nature are either fermions with half-integer spin or bosons with integer spin. Fermions are subject to Pauli's exclusion principle which tells us that every quantum state in a system can be occupied by only one identical fermion. Bosons on the other hand do not obey this law, they follow Bose statistics instead. The total wavefunction of a fermionic system is antisymmetric with respect to particle exchange while a bosonic system has a symmetric total wavefunction.

Every particle can be described as a wave packet of the size of the de Broglie wavelength $\lambda_{\mathrm{dB}} = hc/E$ where E is the particle's energy, h is Planck's constant and c is the speed of light. In a thermal ensemble the mean de Broglie wavelength is related to the temperature of the ensemble and we can define the thermal de Broglie wavelength of

the system as

$$\lambda_T = \sqrt{\frac{2\pi\hbar^2}{mk_BT}} \tag{2.1}$$

with $2\pi\hbar = h$ Planck's constant, m the particle mass, k_B the Boltzmann constant and T the temperature of the system. From the dependence of the thermal de Broglie wavelength on the temperature $\lambda_T \propto T^{-1/2}$ it follows that the wave packets describing the atoms in a gas grow smaller the higher the temperature. At room temperature the de Broglie wavelength is on the order of 10^{-12} m which is even smaller than an atom ($\sim 10^{-10}$ m). In this regime any atomic gas can be described as a system of distinct hard balls and the distinction between bosons and fermions has no effect. At a temperature where the de Broglie wavelength is comparable to the distance between the atoms the wave packets begin to overlap. Here the classical description breaks down and the atomic gas reveals its quantum statistical behavior. Now it becomes important whether a system is bosonic or fermionic in nature since this strongly affects its quantum mechanical properties.
In the following we discuss the basic aspects of the behavior of non-interacting bosons and fermions at low temperature.

2.1.1 Bosons

The quantum statistics of bosons are described by the Bose-Einstein distribution:

$$f_B(\mathbf{r},\mathbf{p}) = \frac{1}{\exp\left(\frac{p^2/2m+V(\mathbf{r})-\mu}{k_BT}\right)-1} \tag{2.2}$$

where $\mathbf{r},\mathbf{p}$ and m are the particle's position, momentum and mass, $V(\mathbf{r})$ is the external potential and μ the chemical potential. The value of f_B is the mean occupation number of the quantum state with energy ε_k fulfilling the Schrödinger equation $\left(p^2/2m + V(\mathbf{r})\right)\psi_k = \varepsilon_k\psi_k$.
The Bose-Einstein distribution allows for more than one particle in the same quantum state, there is however a maximum number of particles in excited states $N_{\text{ex,max}}$ depending on the temperature of the system. This follows from the condition that the occupation number of any state cannot be negative and thus $\mu \leq \varepsilon_k \leq \varepsilon_0$ has to hold

for the chemical potential. It is [Pit08]

$$N_{\text{ex,max}} = \sum_{k=0}^{\infty} \frac{1}{\exp\left(\frac{\varepsilon_k - \varepsilon_0}{k_B T}\right) - 1}. \tag{2.3}$$

If the total number of particles N exceeds this limit all other particles have to go into the ground state. Thus for sufficiently small temperature the particles accumulate in the ground state where they form a coherent cloud of atoms, which is called a Bose-Einstein condensate (BEC).

For a Bose gas in a harmonic trap with trap frequencies ω_i the external potential reads

$$V(\mathbf{r}) = \frac{1}{2} m\omega_x^2 x^2 + \frac{1}{2} m\omega_y^2 y^2 + \frac{1}{2} m\omega_z^2 z^2. \tag{2.4}$$

In such a trap the critical temperature for Bose-Einstein condensation is calculated from the condition $N \geq N_{\text{ex,max}}$ and is given by [Pet02]

$$T_c = \frac{\hbar\bar{\omega}}{k_B} \left(\frac{N}{\zeta(3)}\right)^{1/3} \approx 0.94 \, \frac{\hbar\bar{\omega}}{k_B} \, N^{1/3} \tag{2.5}$$

where $\bar{\omega} = (\omega_x \omega_y \omega_z)^{1/3}$ is the average trap frequency and $\zeta(3) \approx 1.202$ is Riemann's zeta function $\zeta(x) = \sum_{k=1}^{\infty} k^{-x}$.

In a Bose-Einstein condensate the bosons cannot be treated as single particles with distinct wave packets anymore, instead they form a single matter wave which exhibits quantum mechanical behavior on a macroscopic scale. The wavefunction of the BEC is just given by the single-particle ground state scaled with the number of condensed particles N_0:

$$\Psi_{\text{BEC}} = \prod_{i=1}^{N_0} \psi_0 e^{i\varphi_i} \tag{2.6}$$

where φ_i is the phase of each single-particle wavefunction. For a non-interacting system the spatial density distribution is also given by the wavefunction of the single-particle ground state:

$$n(\mathbf{r}) = N_0 |\psi_0|^2. \tag{2.7}$$

The number of condensed particles in the system can be deduced from $N_0 = N -$

$N_{\mathrm{exc}}(T)$. For a bosonic gas in a harmonic trap this yields [Pet02]

$$N_0 = N\left[1 - \left(\frac{T}{T_c}\right)^3\right]. \tag{2.8}$$

We see that in the limit of zero temperature all the particles in the system are condensed in the BEC, whereas for $T > 0$ a thermal fraction remains.

2.1.2 Fermions

Fermions have a different quantum statistical behavior than bosons. They are subject to the Pauli principle, which states that every quantum state can be occupied by only one identical fermion. The mean occupation number in a fermionic system is given by the Fermi-Dirac distribution:

$$f_F(\mathbf{r},\mathbf{p}) = \frac{1}{\exp\left(\frac{p^2/2m+V(\mathbf{r})-\mu}{k_B T}\right)+1}. \tag{2.9}$$

In the limit of zero temperature all states with an energy smaller than the chemical potential are occupied by one fermion, it is $f(\mathbf{r},\mathbf{p}) = 1$, all states above that are unoccupied and hence $f(\mathbf{r},\mathbf{p}) = 0$ (see Figure 2.1).
The energy of the highest occupied state is called the Fermi energy $E_F = \mu(T = 0)$. It is related to the number of particles in the system, which can be calculated by integrating $f(\mathbf{r},\mathbf{p})$ over all possible $\mathbf{r}$ and $\mathbf{p}$:

$$N = \frac{1}{2\pi\hbar}\iint f(\mathbf{r},\mathbf{p})d\mathbf{r}d\mathbf{p} \tag{2.10}$$

where $1/2\pi\hbar$ is the spacing of states in phase space, i.e. the density of states.
For a Fermi gas in a harmonic trap the Fermi energy is given by

$$E_F = (6N)^{1/3}\hbar\bar{\omega} \tag{2.11}$$

where $\bar{\omega} = (\omega_x\omega_y\omega_z)^{1/3}$ is again the average trap frequency.
The spatial density and momentum distribution of an ideal, non-interacting Fermi

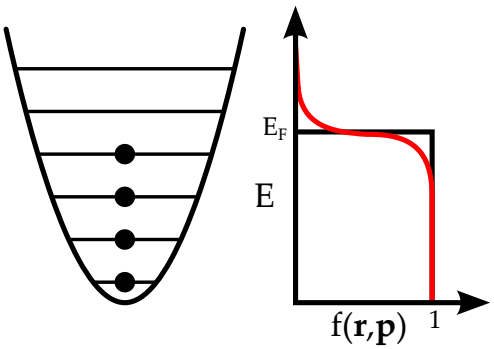

Figure 2.1: Sketch of the Fermi-Dirac distribution at zero temperature (black curve) and $T > 0$ (red curve) and the resulting occupation of quantum states in a harmonic trap filled with fermions. Every quantum state can be occupied by only one identical fermion, thus for $T = 0$ all states up to the Fermi energy E_F are filled, all states with higher energy are empty. For non-zero temperature the Fermi-Dirac distribution becomes smooth, states with energy above the Fermi energy now have a non-zero probability to be occupied while states below E_F have an occupation probability smaller than unity.

gas can be calculated by integrating Equation 2.9 over **r** and **p**, respectively [Gio08]:

$$n(\mathbf{r}) = \frac{1}{2\pi\hbar}\int f(\mathbf{r},\mathbf{p})d\mathbf{p} \xrightarrow{T\to 0} \frac{8N}{\pi^2 x_F y_F z_F}\left(1-\frac{x^2}{x_F^2}-\frac{y^2}{y_F^2}-\frac{z^2}{z_F^2}\right) \tag{2.12}$$

$$n(\mathbf{p}) = \frac{1}{2\pi\hbar}\int f(\mathbf{r},\mathbf{p})d\mathbf{r} \xrightarrow{T\to 0} \frac{8N}{\pi^2 p_F^3}\left(1-\frac{p^2}{p_F^2}\right). \tag{2.13}$$

Here we have used the relation $E_F = \frac{p_F^2}{2m} = \frac{1}{2}m\left(\omega_x^2 x_F^2 + \omega_y^2 y_F^2 + \omega_z^2 z_F^2\right)$. From this we see that the momentum distribution of a non-interacting Fermi gas in a trap is isotropic even if the trap itself is not. Anisotropic expansion of an atomic cloud released from its trap would thus be a sign of interaction effects in the Fermi gas. More specifically, hydrodynamic behavior of a Fermi gas in an anisotropic trap leads to an inversion of the aspect ratio of the cloud during time-of-flight [O'H02, Tre11].

2.2 Introducing interactions — Scattering at low temperatures

The key to understanding the behavior of any physical system is to understand its inter-particle interactions. In atomic gases interactions are mediated by collisions, hence it is important to examine the scattering properties of such systems.

In general one needs to distinguish between elastic collisions between two atoms which allow the gas to thermalize and inelastic collisions which lead to particle loss. The only inelastic process open to two atoms in an ultracold Fermi gas is a spin-changing collision. Fortunately, in our system it is possible to prepare the atoms in states where spin-changing collisions are suppressed due to energy and momentum conservation. In that case the most important kind of inelastic collision is three-body loss where two atoms form a deeply bound molecule while the third scattering partner carries away the binding energy as kinetic energy and all three are lost from the trap.

It is now quite intuitive to understand that the rate of elastic collisions in an atomic gas should scale with the square of the density n, since there are two particles involved in the process, whereas inelastic collisions scale with n^3, if we can prepare the atoms in states which are stable against dipolar relaxation. This scaling with density means that there is an upper limit for the density below which elastic collisions dominate over inelastic ones, or in other words the thermalization rate is larger than the rate for three-body loss. This is a necessary requirement for trapping and cooling of atomic gases.

However, this need to have a dilute system is also the reason why atomic quantum gases have to be "ultracold". From Equation 2.5 we know that the critical temperature for quantum degeneracy grows with the number of particles in the system and hence, for a constant trap volume, with the density of the gas:

$$T_c \propto n^{1/3}. \tag{2.14}$$

This means that if the gas is too dilute T_c becomes experimentally inaccessible, thus the gas has to be sufficiently dense to allow us to observe quantum effects. Typical densities where both constraints, small three-body loss rates and high T_c, are met lie in the range of $n \sim 10^{12} - 10^{15}\,\mathrm{cm}^{-3}$ depending on the atomic species [SK11].

When considering scattering in an ultracold Fermi gas we can therefore assume the limit of low temperature, i.e. low energy of the scattering particles, and large inter-particle spacing. Fortunately in this regime scattering is rather simple to describe using a single parameter, the scattering length a. The simplicity of interactions in ultracold quantum gases is in fact one important reason why they are so successful in the study of fundamental quantum mechanical phenomena. In the following section we will introduce the concept of the scattering length and discuss its importance.

2.2.1 Two-body scattering in a spherically symmetric potential

In a two-body scattering event we can separate center-of-mass and relative motion and only need to solve the Schrödinger equation describing one particle with the reduced mass $\mu_r = m/2$ scattering off the potential $V(\mathbf{r})$:

$$\left(-\frac{\hbar^2}{2\mu_r}\nabla^2 + V(\mathbf{r})\right)\psi_{\mathbf{k}}(\mathbf{r}) = E_k\psi_{\mathbf{k}}(\mathbf{r}) \tag{2.15}$$

with a positive energy $E_k = \frac{\hbar^2 k^2}{2\mu_r}$. If, as in our case, the potential is a spherically symmetric short-range potential with a range r_0 the solution in the asymptotic region $r \gg r_0$ reads

$$\psi_{\mathbf{k}}(\mathbf{r}) \propto e^{i\mathbf{kr}} + f(k,\theta)\frac{e^{ikr}}{r}. \tag{2.16}$$

The physical interpretation of this is the superposition of an incoming plane wave and an outgoing scattered spherical wave with wavevector $\mathbf{k}$. The function $f(k,\theta)$ is the scattering amplitude, which is the probability amplitude for the particle to be scattered in the direction $\mathbf{r}/r$ under an angle θ with respect to its initial direction $\mathbf{k}/k$. The scattering amplitude contains all the information about the scattering event and is related to the differential cross section:

$$\frac{d\sigma}{d\Omega} = |f(k,\theta)|^2. \tag{2.17}$$

However, this is only true for distinguishable particles. If the scattering particles are identical both scattering processes shown in Figure 2.2 yield the same result and thus both have to be considered in the calculation of the scattering wavefunction.

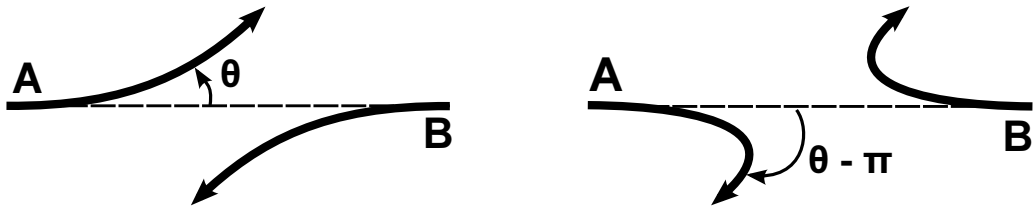

Figure 2.2: Two scattering processes which have the same result if the particles A and B are identical. Picture adapted from [Dal98]

For bosons (fermions) the wavefunction has to be (anti-)symmetric under particle exchange such that Equation 2.16 becomes

$$\psi_{\mathbf{k}}(\mathbf{r}) \propto \underbrace{\frac{1}{\sqrt{2}}\left(e^{i\mathbf{kr}} \pm e^{-i\mathbf{kr}}\right)}_{\text{incoming plane wave}} + \underbrace{\frac{1}{\sqrt{2}}\left[f(k,\theta) \pm f(k,\pi-\theta)\right]\frac{e^{ikr}}{r}}_{\text{scattered wave}} \tag{2.18}$$

with the plus sign for bosons and the minus for fermions, respectively. Considering this the differential cross section for bosons (fermions) is then given by the sum (difference) of the two interfering terms:

$$\frac{d\sigma}{d\Omega} = \begin{cases} |f(k,\theta)|^2 & \text{for distinguishable particles} \\ |f(k,\theta) + f(k,\pi-\theta)|^2 & \text{for identical bosons} \\ |f(k,\theta) - f(k,\pi-\theta)|^2 & \text{for identical fermions.} \end{cases} \tag{2.19}$$

Since the scattering potential is spherically symmetric we can write $\psi_{\mathbf{k}}(\mathbf{r})$ in spherical coordinates and expand it in terms of partial waves with angular momentum l:

$$\psi_{\mathbf{k}}(\mathbf{r}) = \sum_{l=0}^{\infty} \frac{u_l(r)}{r} P_l(\cos\theta) \tag{2.20}$$

with $P_l(x)$ being the Legendre polynomials. Solving this for $u_l(r)$ yields

$$u_l(r) \propto sin\left(kr - \frac{l\pi}{2} + \delta_l\right) \tag{2.21}$$

which corresponds to the incoming wave with a phase shift δ_l acquired in the scattering event.
If we now use this in Equation 2.20 and compare the result with Equation 2.16 we get for the scattering amplitude [Wac05]

$$f(k,\theta) = \frac{1}{k}\sum_{l=0}^{\infty}(2l+1)e^{i\delta_l}\sin\delta_l P_l(\cos\theta) \tag{2.22}$$

and for the cross section using Equation 2.19 and integrating over Ω [Dal98]:

$$\sigma = \begin{cases} \frac{4\pi}{k^2}\sum_{l=0}^{\infty}(2l+1)sin^2(\delta_l) & \text{for distinguishable particles} \\ \frac{8\pi}{k^2}\sum_{l\text{ even}}(2l+1)sin^2(\delta_l) & \text{for identical bosons} \\ \frac{8\pi}{k^2}\sum_{l\text{ odd}}(2l+1)sin^2(\delta_l) & \text{for identical fermions.} \end{cases} \tag{2.23}$$

Due to the (anti-)symmetry of the Legendre polynomials for even (odd) angular momentum $P_l(\cos\theta) = (-1)^l P_l(\cos(\pi-\theta))$ all odd (even) terms cancel out in the calculation of Equation 2.19 while all even (odd) terms gain a factor of two.

2.2.2 The limit of low energy and the scattering length

Considering that the scattering phase shift for small k behaves like $\delta_l \propto k^{2l+1}$ [Wac05] we see that for low energy (small k) only partial waves with angular momentum $l = 0$ contribute to the scattering process and all other terms $l > 0$ can be neglected. In this case of pure s-wave scattering we have

$$f(k,\theta) = \frac{1}{k}e^{i\delta_0}\sin(\delta_0). \tag{2.24}$$

This is independent of θ, thus the scattering amplitude is isotropic for small energy.
All the information about the scattering event is now contained in the wavevector k and the phase shift δ_0. Since we are in the low energy limit we can expand δ_0 in terms

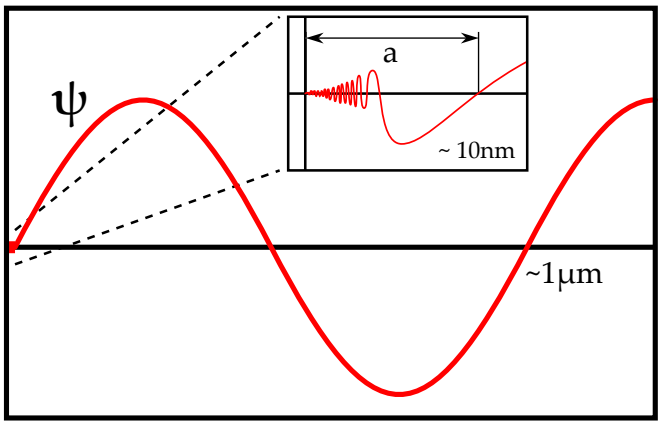

Figure 2.3: The graph shows the scattered wave at long range. The inset shows the short-range effect of the scattering process on the wavefunction. It illustrates the definition of the scattering length as the distance the wave function is pushed out of the scattering center by the acquired phase shift. Picture adapted from [Wei09].

of k^2 and truncate the expansion after the first order:

$$k \cot \delta_0(k) = -\frac{1}{a} + \frac{1}{2} r_e k^2 + \ldots \approx -\frac{1}{a}. \tag{2.25}$$

This serves as the definition of the effective range of s-wave scattering r_e and the scattering length a. In the limit $k \to 0$ the latter is defined as

$$a = -\frac{\tan \delta_0}{k}. \tag{2.26}$$

The scattering length corresponds to the distance the wavefunction gets pushed out of the scattering center due to the phase shift it acquires in the scattering event. This is illustrated in Figure 2.3.

Now we can determine the scattering cross section (Equation 2.23) in terms of this new parameter:

$$\sigma = \begin{cases} \frac{4\pi a^2}{1+k^2a^2} & \text{for distinguishable particles} \\ \frac{8\pi a^2}{1+k^2a^2} & \text{for identical bosons} \\ 0 & \text{for identical fermions.} \end{cases} \tag{2.27}$$

This is an important result as it shows that identical fermions at low temperatures do

not interact. Hence in order to prepare an ultracold fermionic system with interactions we need to use atoms in two different spin states. In that case we can apply the result for distinguishable particles.
In the limit $ka \ll 1$ Equation 2.27 yields

$$\sigma_{dist} = 4\pi a^2 \tag{2.28}$$

for distinguishable particles. This is just the classical scattering cross section of hard spheres with radius a. With our system we usually are in this regime, where the de Broglie wavelength $\lambda_{\mathrm{dB}} = 2\pi/k$ is much larger than the scattering length. However in an ultracold gas it is also possible to reach the regime where $ka \gg 1$ and thus $a \gg \lambda_{\mathrm{dB}}$. In this case the scattering cross section becomes independent of the scattering length and for distinguishable particles is given by

$$\sigma = \frac{4\pi}{k^2}. \tag{2.29}$$

2.2.3 Mean field interaction

When two atoms approach each other in a scattering event their wavefunction varies rapidly on short range which is difficult to calculate. However, as we have said before, in the limit of low energy the scattering process depends only on the scattering length. Then we can neglect the short-range correlations and sum up their effect in the distance the wavefunction is pushed out of the scattering center (see inset in Figure 2.3). We can introduce an effective interaction per particle which characterizes the scattering and depends on the scattering length a [Pet02]. Multiplying this with the density yields the mean-field energy of the system:

$$E_{\mathrm{int}} \sim \frac{4\pi\hbar^2 a}{m} k_F^3 \tag{2.30}$$

where we have used that the inter-particle spacing $n^{-1/3}$ in a degenerate quantum gas is comparable to the de Broglie wavelength and thus it is $n \sim k_F^3$.
To identify the regimes of weak and strong interaction we can compare this mean-field interaction energy with the relevant energy scale of our system, the Fermi energy

$E_F = \hbar^2 k_F^2 / 2m$. This is equivalent to considering the dimensionless parameter $k_F a$.
For $k_F a \ll 1$ we have $E_{\text{int}} \ll E_F$ and every scattering event has only a small effect on the system. This is the regime of weak interactions. Here the scattering cross section is given by Equation 2.28.
On the other hand, when mean-field and Fermi energy become comparable and it is $k_F a \approx 1$, interactions dominate the system. For $k_F a \gg 1$ the gas is in the so-called unitary regime. The cross section is now given by Equation 2.29, thus the scattering length drops out of the problem and the physics becomes independent of length scales. This tells us that once we have reached the unitary regime, further enhancing the scattering length will not lead to stronger interactions.
More information on scattering can be found in the literature [Sch05, Wac05, Gio08, Dal98].

2.3 Tuning interactions — The Feshbach resonance

One of the key features of ultracold atomic gases is the tunability of their inter-particle interactions. This is made possible by so-called Feshbach resonances where the scattering length diverges. In the following we will discuss the basic physics of this phenomenon, more thorough studies can be found in [Chi10, Ket08].
Before and after a collision the scattering partners are in a quantum state described by the internal state of the atoms and the interaction potential between them. For example this could be a spin polarized triplet state of two ^{6}Li atoms in an external magnetic field interacting via a van-der-Waals potential. Such a quantum state is called a scattering channel. We distinguish between open and closed channels depending on whether the atoms are allowed to poulate the scattering channel or whether this is energetically forbidden. If the incoming channel, which is open by definition, is the only open channel the atoms come close to each other, scatter and leave again in the same channel. In such a scattering event the atomic wavefunction acquires a constant phase shift which gives rise to the background scattering length associated with the scattering process.
If there is a closed scattering channel present the atoms cannot populate it. Nevertheless, if there is a coupling between the open and closed channel and the closed channel supports a bound state close to the energy of the two incoming atoms (in

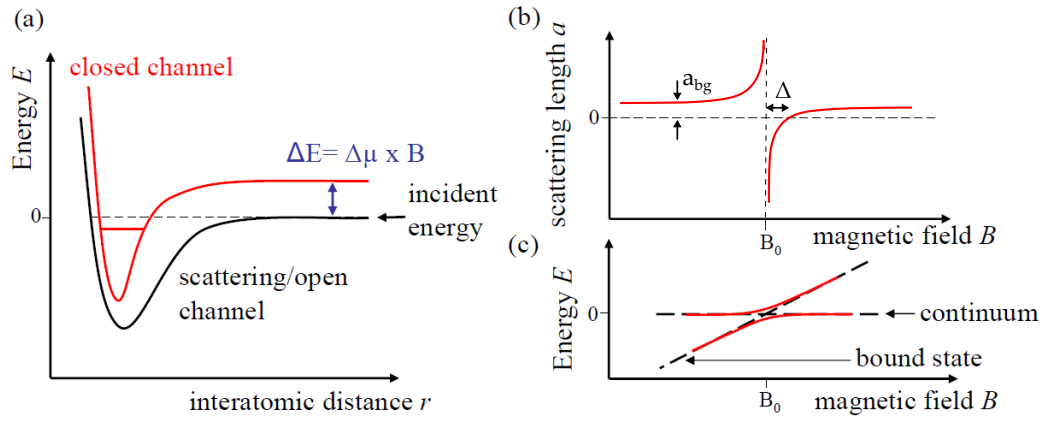

Figure 2.4: Origin of a Feshbach resonance. a) Sketch of a two-channel system including an open channel (black) and a closed one (red) which supports a bound state close to the continuum of the open channel. The binding energy of the bound state can be tuned with respect to the open channel by applying an external magnetic field. b) When the bound state is tuned to coincide with the incident energy of the scattering atoms the scattering length diverges. c) The coupling induces an avoided crossing of the open channel continuum and the closed channel molecular state on resonance. This allows to transform two free atoms into a molecule and vice versa by ramping across the Feshbach resonance.

ultracold gases this can usually be approximated as zero energy) the scattering event is influenced by the presence of this bound state. The coupling of the open channel to the bound state in the closed channel induces a further phase shift to the scattering wavefunction which changes the scattering length. A sketch of such a scattering scenario is shown in Figure 2.4.

If the scattering channels have different magnetic moments one can tune the binding energy of the bound state with respect to the continuum energy of the open channel by changing the external magnetic field. In ^{6}Li such an open channel is a spin polarized triplet state $|\uparrow\uparrow\rangle$ with magnetic moment $\mu_{\uparrow\uparrow} = \mu_B$ while the closed channel bound state is a singlet state $|\uparrow\downarrow\rangle$ with $\mu_{\uparrow\downarrow} = 0$. If the bound state coincides with the incident energy of the scattering atoms the scattering length is resonantly enhanced. This divergence of a is called a Feshbach resonance.

The behavior of the scattering length in dependence of the external magnetic field is

shown in Figure 2.4b and is mathematically described by

$$a(B) = a_{bg}\left(1 - \frac{\Delta}{B - B_0}\right) \tag{2.31}$$

with a_{bg} the background scattering length and Δ and B_0 the width and position of the resonance, respectively. The width of a Feshbach resonance is defined as the difference in magnetic field between B_0 and the zero-crossing of a.
Figure 2.4c shows the change of the binding energy of the closed channel molecular state with respect to the open channel continuum across the Feshbach resonance:

- $B < B_0$: Below resonance the bound state lies below the closed channel continuum as depicted in Figure 2.4a, the scattering length is positive and the interaction between the atoms in an ultracold Fermi gas is effectively repulsive. This side of the resonance is called the BEC side, since the atoms can form molecules and these can condense into a molecular Bose-Einstein condensate (see Chapter 5).

- $B = B_0$: On resonance the energies of bound state and open channel continuum are degenerate and the scattering length diverges. The coupling induces an avoided crossing of the open channel continuum and the closed channel bound state. This enables the transformation of free atoms into molecules and vice versa by adiabatically ramping across the Feshbach resonance.

- $B > B_0$: On the BCS side of the Feshbach resonance the bound state sits above the open channel continuum, the scattering length takes negative values and the atoms experience an attractive mean-field interaction. As described by BCS-theory the atoms form Cooper pairs and become superfluid [Bar57].

The fact that we can use Feshbach resonances to tune the interaction between atoms in an ultracold quantum gas gives us unique control over the behavior of the system. This is one of the reasons why ultracold atomic gases are so successful in the study of fundamental few- and many-body systems today.

2.3.1 Weakly bound dimers

On the BEC side of the Feshbach resonance the bound state in the closed scattering channel has lower energy than the state of two free atoms in the open channel continuum. For magnetic fields far below the Feshbach resonance this molecular state is so deeply bound that we cannot detect it with our imaging systems. Close to resonance however it is a weakly bound dimer state with universal properties. Its binding energy depends on the scattering length a and is given by [Pet04]

$$E_B = \frac{\hbar^2}{ma^2}. \tag{2.32}$$

The size of the weakly bound dimers is on the order of a.

As this weakly bound dimer state is important for our experiments with gases of ultracold ^{6}Li, e.g. for the preparation of a molecular Bose-Einstein condensate (see Chapter 5), we will now examine its scattering properties and stability.

Just as we have derived a scattering length to describe collisions between free atoms in the gas one can find scattering lengths associated with the interactions between a dimer and a free atom and two dimers. These atom-dimer and dimer-dimer scattering lengths are directly related to the atom-atom scattering length [Pet04, Pet05]:

$$a_{ad} = 0.6\,a \tag{2.33}$$

$$a_{dd} = 1.2\,a. \tag{2.34}$$

As $a > 0$ on the BEC side of the resonance, the interactions of atoms with dimers and dimers with each other are repulsive.

The stability of the dimers is determined by the rate of atom-dimer and dimer-dimer collisions in which the dimer can relax into a deeply bound state. In a two-component Fermi gas such a collision necessarily includes at least two identical fermions which do not interact (see Equation 2.27). If the dimer is deeply bound it behaves like a composite boson and the relaxation into a lower-lying state is allowed. However, in a weakly bound dimer the constituents are resolved in the collision and the relaxation is suppressed by Pauli blocking. Thus the dimer is more stable the smaller its binding energy. D. Petrov et al. determined from this suppression a dependence of the

relaxation rate constant on the scattering length [Pet04]:

$$\alpha_{rel} = a^{-s}. \tag{2.35}$$

For collisions involving a weakly bound dimer and one free atom the parameter $s = 3.33$ while for dimer-dimer scattering it is $s = 2.55$. Both relaxation processes consequently are more strongly suppressed for larger a which means that the gas gains stability for stronger interactions.
Another important parameter is the ratio of this relaxation rate to the rate of elastic collisions in the gas. For ^{6}Li this can take values of $\alpha_{rel}/\alpha_{el} \sim 10^{-4}$ which is uniquely small for a Fermi gas. This makes it possible to prepare long-lived molecular samples and conduct experiments.

2.4 Properties of ^{6}Li

For our experiments we use ^{6}Li atoms. In this section we give an overview of the properties of ^{6}Li which are important for optical trapping and cooling of this atomic species. All of the information given here and much more can be found in [Geh03, Chi10].

2.4.1 Level structure

^{6}Li belongs to the group of alkali metals which means that it has only one valence electron. Hence its spin quantum number is $S = 1/2$ and its energy spectrum is relatively simple (Figure 2.5). Its nuclear spin is $I = 1$, hence ^{6}Li has a half-integer total spin quantum number making it a fermion.
For trapping and cooling purposes we use the D2 transition from the electronic ground state $2^2S_{1/2}$ to the $2^2P_{3/2}$ state at a wavelength of approximately 671nm. The $2^2S_{1/2}$ state is split into two, the $2^2P_{3/2}$ state into three hyperfine substates with a splitting of 228.2MHz and only 4.4MHz respectively (see Figure 2.5). As the D2 transition has a natural linewidth of 5.9MHz, the hyperfine structure of the $2^2P_{3/2}$ state is not resolved. Thus we can address two transitions $\{\, ^2S_{1/2},\ F = 3/2 \,\} \rightarrow {}^2P_{3/2}$ and $\{\, ^2S_{1/2},\ F = 1/2 \,\} \rightarrow {}^2P_{3/2}$ called cooler and repumper, respectively. This yields a closed cycle

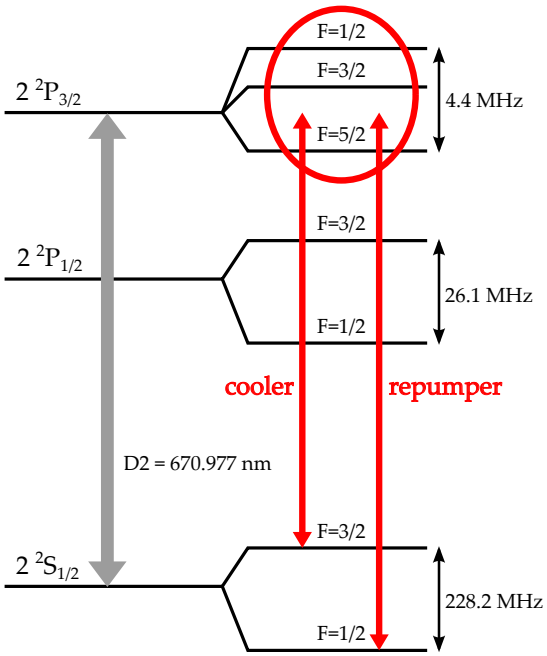

Figure 2.5: Level scheme of ^{6}Li. For trapping and cooling of the atoms we use the D2 transition. As the hyperfine splitting of the $2^2P_{3/2}$ state cannot be resolved we can address two transitions labeled cooler and repumper which couple the resolved hyperfine states of the ground state to the hyperfine manifold of the $2^2P_{3/2}$ state in a closed cycle. Picture adapted from [Geh03]

between the ground and second excited state.

Under the influence of a homogeneous external magnetic field the hyperfine structure of the $2^2S_{1/2}$ state is split up according to magnetic quantum number as shown in Figure 2.6. In the low field regime electron spin S and nuclear spin I couple to the new quantum number $F = S + I = \{1/2, 3/2\}$. The Zeeman effect then splits up the states according to the magnetic quantum number $m_F = \{-F, .., F\}$ into six states $|F, m_F\rangle$ which we label $|1\rangle$ to $|6\rangle$. In the high field regime – for ^{6}Li this is reached already at magnetic fields of 30 G and higher – F no longer is a good quantum number and S and I decouple. Following the Paschen-Back effect the six states $|S, I, m_S, m_I\rangle$ are split into two groups with three states $m_I = 0, \pm 1$ each. The three states with $m_S = +1/2$ ($|4\rangle$ to $|6\rangle$) are low-field seekers, their energy is higher at larger magnetic fields. On the other hand the three states with $m_S = -1/2$ ($|1\rangle$ to $|3\rangle$) are high-field seekers, their energy is minimized for strong external fields. Mixtures of atoms in states $|4\rangle$, $|5\rangle$ and

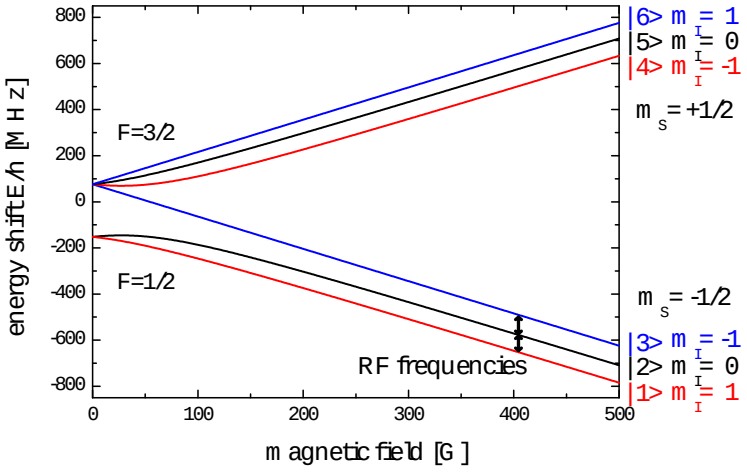

Figure 2.6: Magnetic splitting of the hyperfine states of ^{6}Li in the ground state $2^2S_{1/2}$. The states $|4\rangle$ - $|6\rangle$ are high-field seekers, the states $|1\rangle$ - $|3\rangle$ are low-field seekers. The latter ones are the states we use in our experiments.

$|6\rangle$ are unstable and decay into the states $|1\rangle$, $|2\rangle$ and $|3\rangle$ via spin-changing collisions. Mixtures of atoms in the three lower states cannot decay in two-body collisions due to the laws of energy and momentum conservation, thus they can be used for the preparation of an atomic Fermi gas.
Hence, we do experiments with atoms in states $|1\rangle$, $|2\rangle$ and $|3\rangle$. To transfer atoms between these three states we use radio frequency signals to flip their nuclear spin. The energy differences between the states (see Figure 2.6) are approximately $\Delta E_{12} \approx 2\pi\hbar \cdot 76\,\mathrm{MHz}$ and $\Delta E_{23} \approx 2\pi\hbar \cdot 82\,\mathrm{MHz}$ around 750 G which is a typical value for the magnetic offset field in our experiments.

2.4.2 Feshbach resonances

In a Fermi gas with three spin components there is a scattering length describing the interactions between each of the two components. In ^{6}Li a_{12}, a_{13} and a_{23} all diverge at a Feshbach resonance in roughly the same magnetic field region (see Figure 2.7).
All s-wave Feshbach resonances between ^{6}Li atoms in states $|1\rangle$, $|2\rangle$ and $|3\rangle$ at experimentally accessible magnetic fields are listed in Table 2.1. The three Feshbach resonances shown in Figure 2.7 each have an unusually large width which allows for

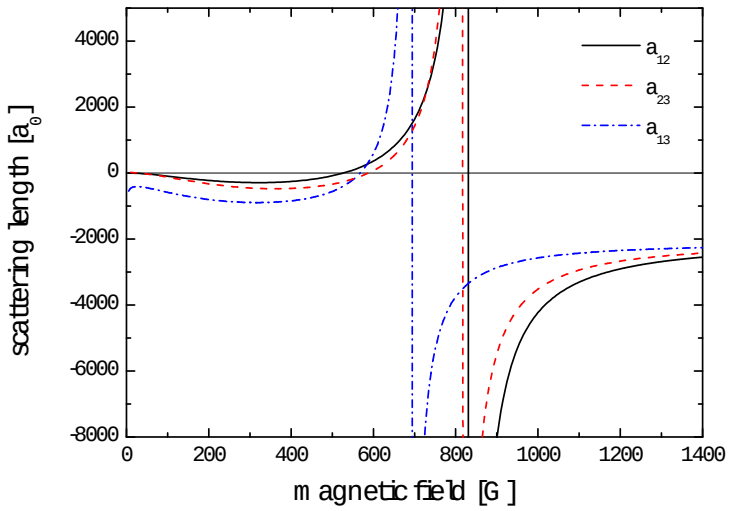

Figure 2.7: Scattering lengths a_{ij} of ^{6}Li between atoms in the three lowest hyperfine states as a function of the magnetic field strength.

greater accuracy in tuning the interaction potential between the atoms. It also leads to an overlap of the resonances of the three different spin mixtures. This overlap is a feature unique in ^{6}Li and means that the interactions between all components in a three-component Fermi gas are resonantly enhanced in the same magnetic field region. Only for this reason is it possible to produce a strongly interacting three-component Fermi gas with ^{6}Li.

s-wave Feshbach resonances of ^{6}Li		
interacting states	resonance position	width
$\|1\rangle$-$\|2\rangle$	834 G	-300 G
	543 G	0.1 G
$\|1\rangle$-$\|3\rangle$	690 G	-122.3 G
$\|2\rangle$-$\|3\rangle$	811 G	-222.3 G

Table 2.1: Positions and widths of the s-wave Feshbach resonances in ^{6}Li between atoms in states $|1\rangle$-$|3\rangle$. Additionally there are four p-wave resonances. These are not listed here as they are not important in our measurements. Numbers are taken from [Chi10].

3 Optical dipole traps

Contents

So far we have discussed how atoms behave and interact at low temperature. In order to prepare such a system, we need to confine the atoms in space and cool them down from several hundred Kelvin to temperatures in the Nanokelvin range. This cannot be done in one step, instead we need to employ a number of cooling schemes and confine the atoms in different traps for different temperature ranges. Most of the work done in the course of this thesis was concerned with the development and setup of different optical dipole traps. Hence in this chapter we will discuss the working principle and properties of optical dipole traps before presenting the key design goals for the traps in our experiment.

3.1 Essential properties of optical dipole traps

As their name implies optical dipole traps use the electric dipole interaction between atoms and the strong electric field of a laser beam to spatially confine atoms. Large detuning of the trapping light with respect to the atomic transition ensures that the scattering of photons and optical excitations of the atoms are negligible compared to the dipole force.

In the following we use a classical model to derive the main equations governing optical dipole traps [Gri00]. As ^{6}Li is an alkali atom with a single valence electron, it can be treated as a classical oscillator with an eigenfrequency ω_0 equal to the frequency of the optical transition. In this classical picture the laser light is treated as an electric

field oscillating with the frequency ω:

$$\mathbf{E}(\mathbf{r},t) = \hat{e}\left(E_0(\mathbf{r})e^{-i\omega t} + E_0^*(\mathbf{r})e^{i\omega t}\right) \tag{3.1}$$

where $\hat{e}$ is the unit vector of the polarization of the light. This classical approach is a good approximation if the atomic transition is strongly dipole allowed and the laser light is far detuned from resonance and thus saturation effects can be neglected.

The atom has no permanent dipole moment since the valence electron occupies an s-orbital. However, if an atom is placed into an electric light field, this field induces an atomic dipole moment which oscillates with the frequency ω of the light and depends on the complex polarizability $\alpha(\omega)$ of the atom:

$$\mathbf{p}(\mathbf{r},t,\omega) = \alpha(\omega)\mathbf{E}(\mathbf{r},t). \tag{3.2}$$

This induced dipole moment in turn interacts with the light field via a dipole potential

$$U_{\text{dip}}(\mathbf{r}) = -\frac{1}{2}\langle \mathbf{pE}\rangle_T = -\text{Re}(\alpha)|E_0(\mathbf{r})|^2 = -\frac{1}{2\epsilon_0 c}\text{Re}(\alpha)I(\mathbf{r}) \tag{3.3}$$

where the angular brackets represent the time average over one oscillation period $T = 2\pi/\omega$, which makes all terms with a factor $e^{\pm 2i\omega t}$ vanish. In the last step we have introduced the intensity of the laser defined as $I = 2\epsilon_0 c|E_0|^2$ with ϵ_0 being the vacuum permittivity and c the speed of light.

The force acting on the atom in the presence of the laser light is then given by the gradient of the dipole potential:

$$\mathbf{F}_{\text{dip}}(\mathbf{r}) = -\nabla U_{\text{dip}}(\mathbf{r}) = \frac{1}{2\epsilon_0 c}\text{Re}(\alpha)\nabla I(\mathbf{r}). \tag{3.4}$$

Hence the atom feels a force proportional to the intensity gradient of the laser beam.

The only unknown parameter left is the polarizability of the atom which we can determine from Larmor's formula for the power radiated by an accelerated charge [Wac05]

$$P(t) = \frac{e^2\ddot{x}(t)^2}{6\pi\epsilon_0 c^3} \tag{3.5}$$

where e is the particle's electric charge and $\ddot{x}(t)$ its acceleration. Here the accelerated particle is the electron oscillating around the atomic core on the trajectory $x(t) = x_0 \sin(\omega t)$. From this we can calculate the average quadratic acceleration over one oscillation $\langle \ddot{x}^2 \rangle_T$ and use it in Equation 3.5. Separating the energy of the harmonic oscillator $E_{\text{ho}} = 1/2 m\omega^2 x_0^2$ we get [Foo07]

$$\langle P \rangle_T = \frac{e^2\omega^2}{6\pi\epsilon_0 m c^3} E_{\text{ho}} = \Gamma_\omega E_{\text{ho}}. \tag{3.6}$$

Here Γ_w is the damping rate of the harmonic oscillator defined as $\dot{E}_{\text{ho}} = -\Gamma_\omega E_{\text{ho}}$. Now we can write down the equation of motion of the electron as a damped harmonic oscillator driven by the force on a charge e in an electric field $\mathbf{F} = -e\mathbf{E}$. Considering that the dipole moment is given by the displacement of the charge $\mathbf{p} = e\mathbf{x}$ we can write the equation of motion in terms of $\mathbf{p}$

$$\ddot{\mathbf{p}} + \Gamma_\omega \dot{\mathbf{p}} + \omega_0^2 \mathbf{p} = -e^2 \frac{\mathbf{E}(\mathbf{t})}{m}. \tag{3.7}$$

Solving this for the polarizability finally yields [Gri00]

$$\alpha(\omega) = 6\pi\epsilon_0 c^3 \frac{\Gamma}{\omega_0} \frac{1}{\omega_0^2 - \omega^2 - i(\omega^3/\omega_0^2)\Gamma} \tag{3.8}$$

where we have introduced the resonant damping rate $\Gamma = (\omega_0/\omega)^2 \Gamma_\omega$ which is equivalent to the lifetime of the excited state. This gives us the final result for the dipole potential an atom experiences in the electric field of a laser:

$$U_{dip}(\mathbf{r}) = -\frac{3\pi c^2}{2\omega_0^3} \left(\frac{\Gamma}{\Delta} + \frac{\Gamma}{\Delta + 2\omega_0} \right) I(\mathbf{r}). \tag{3.9}$$

This expression diverges at the resonance frequency ω_0 where the detuning $\Delta = \omega - \omega_0$ vanishes. If the detuning is much smaller than the resonance frequency $|\Delta| \ll \omega_0$ the second term can be neglected and we get

$$U_{dip}(\mathbf{r}) = \frac{3\pi c^2}{2\omega_0^3} \frac{\Gamma}{\Delta} I(\mathbf{r}). \tag{3.10}$$

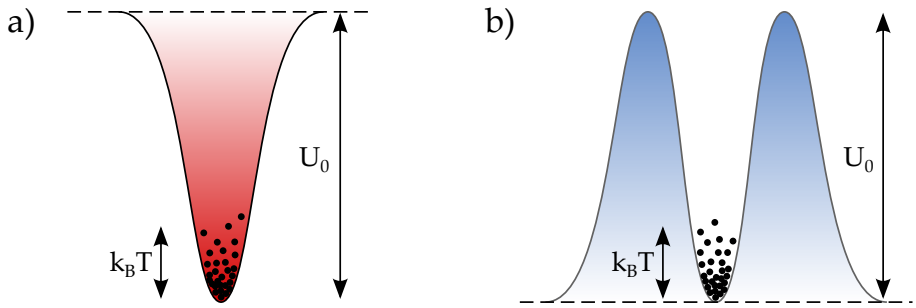

Figure 3.1: Illustration of optical dipole traps with red (a) and blue (b) detuning. The trap depth U_0 is given by the dipole potential and atoms are pulled toward potential minima. On the left side the laser is red detuned and atoms are trapped in the center of a Gaussian beam, on the right side the laser is blue detuned and a "donut" shaped beam can be used to spatially confine the atoms. Picture adapted from [Gri00].

However, the laser light we use for our dipole traps has a wavelength of 1064 nm while the atomic transition lies at approximately 671 nm. Thus we have $|\Delta| \approx 1/2\omega_0$, which means the second term gives a 20 % correction on the dipole potential. Nevertheless we can use Equation 3.10 for some qualitative analysis.
We see that the sign of the potential depends on the sign of the detuning: For red detuned light ($\Delta < 0$) the dipole potential is negative and has its minimum value where the intensity is largest. Thus atoms will be pulled into the laser beam towards the point of maximum intensity. On the other hand if the laser is blue detuned ($\Delta > 0$) the potential minimum is at the point of minimum intensity and atoms will be repelled by the light field, i.e. pushed out of the laser beam. Thus, to spatially confine atoms with an optical dipole trap one can either use light at a frequency below the atomic transition (red detuned) and trap the atoms in the focus of a laser beam with a Gaussian intensity distribution or use light above resonance (blue detuned) and trap them in the center of a "donut" shaped beam (see Figure 3.1). For the dipole traps in our experiment we have chosen the first possibility since a laser beam with Gaussian beam shape is much easier to produce.
The intensity distribution of a laser beam with Gaussian shape traveling in the z-direction is

$$I(x,y,z) = \frac{2P}{\pi w_x w_y} \exp\left(-2\frac{x^2}{w_x^2} - 2\frac{y^2}{w_y^2}\right). \tag{3.11}$$

Here w_x, w_y are the radial distances to the center where the intensity is $1/e^2$ of its

peak value. They depend on the axial coordinate as

$$w_i(z) = w_{0,i}\sqrt{1 + \left(\frac{z}{z_{R,i}}\right)^2} \tag{3.12}$$

with the minimum radius w_0 at the focus, the so-called beam waist, and the Rayleigh range $z_{R,i} = \pi w_{0,i}^2/\lambda$. The beam waists and Rayleigh ranges determine the region of confinement for the atoms, i.e. the trapping volume. The Rayleigh range is always larger than the beam waist resulting in weaker axial than radial confinement. An illustration of such a single beam dipole trap can be seen in Figure 3.2a. The quadratic dependence of z_R on the beam waist limits the trapping volume of the single beam dipole trap. If the beam waists are increased for a larger trapping volume, the aspect ratio increases as well and the confinement in axial direction decreases quadratically. A solution to this problem would be to use a crossed-beam trap (see section 3.2).

If the thermal energy of the sample $k_B T$ is much smaller than the trap depth U_0 the extension of the trapped cloud is even smaller than the trapping volume . This is the case in most of our experiments. Thus we can approximate the center of the Gaussian trap by expanding the exponential to the second order ($x \ll w_i$). This has the form of a three-dimensional harmonic oscillator:

$$U_{dip}(x,y,z) \approx -U_0\left[1 - 2\left(\frac{x}{w_{0,x}}\right)^2 - 2\left(\frac{y}{w_{0,y}}\right)^2 - \left(\frac{z}{z_R}\right)^2\right] \tag{3.13}$$

where U_0 is the trap depth proportional to the peak intensity $I_{max} = 2P/(\pi w_{0,x} w_{0,y})$. The harmonic oscillator frequencies which characterize the trap and give the level spacing in every direction are

$$\omega_{x,y} = \sqrt{\frac{4U_0}{m w_{0,x,y}^2}} \quad \text{and} \quad \omega_z = \sqrt{\frac{2U_0}{m z_R^2}} \tag{3.14}$$

with $\omega_z \ll \omega_{x,y}$. We see that smaller beam waists, i.e. stronger confinement, correspond to larger trap frequencies. The scaling with the laser power goes as $\omega_i \propto \sqrt{P}$.

Similarly to the derivation of the dipole potential above we can calculate the rate with

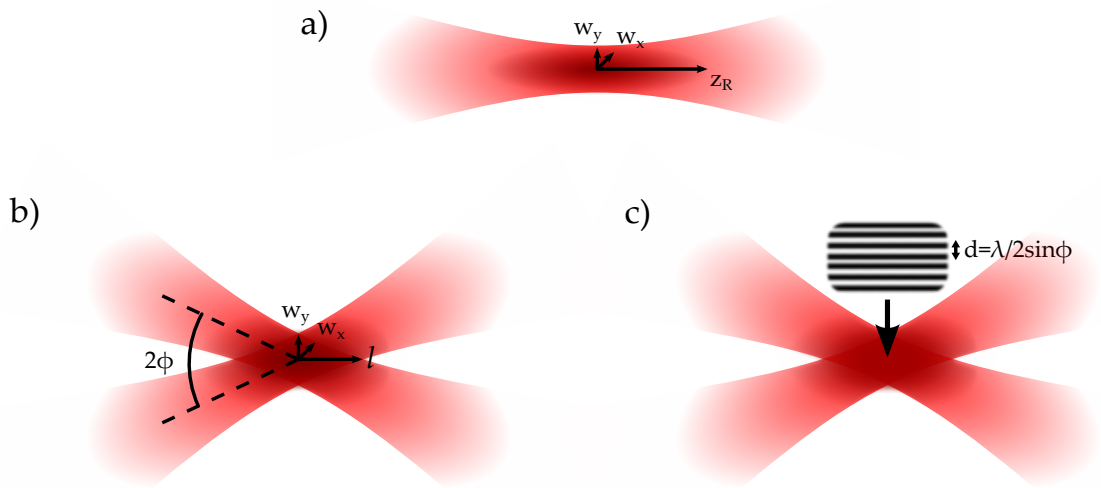

Figure 3.2: Illustration of three different types of red detuned optical dipole traps. a) A single beam trap confines atoms inside its focus. The size of the trapping volume is given by the waists in radial and the Rayleigh range in axial direction. b) Crossed beam trap with orthogonal polarization of the beams: The axial confinement is given by the intersection, thus it is stronger than in a single beam trap. c) Crossed beam trap with parallel polarization: The beams interfere which yields a periodic trapping potential where each interference fringe provides a pancake shaped trap for the atoms. The spacing between the fringes depends on the angle of intersection.

which the atom scatters photons of the light field with energy $\hbar\omega$ [Gri00]:

$$\Gamma_{sc} = \frac{\langle \dot{\mathbf{p}}\mathbf{E} \rangle}{\hbar\omega} \propto \left(\frac{\Gamma}{\Delta} + \frac{\Gamma}{\Delta + 2\omega_0} \right)^2 I(\mathbf{r}) \approx \left(\frac{\Gamma}{\Delta} \right)^2 I(\mathbf{r}) \tag{3.15}$$

Here $\langle \dot{\mathbf{p}}\mathbf{E} \rangle$ is the power absorbed by the atom inside the light field. Γ_{sc} should be be kept small in experiments as it causes heating of the sample. Comparing Equation 3.15 with Equation 3.10 we see that we need a large detuning of the laser to suppress photon scattering which in turn demands large light intensity in order to make the dipole potential sufficiently strong to build deep optical traps.

3.1.1 Evaporative cooling

Once we have trapped atoms inside a dipole trap, for example by transfer from a magneto-optical trap (see Section 4.1.3), we can cool them to degeneracy ($\sim$ 100nK) using a technique called evaporative cooling.

This technique is based on the fact that the temperature of a thermal cloud depends on the mean velocity of the atoms, while the velocities of single atoms follow a thermal distribution. The fastest atoms have more energy than the mean, they occupy higher trap levels and can be found more often outside the center of the trap.

The idea of evaporative cooling is to slowly lower the depth of the trap, i.e. decrease the intensity of the laser, and let the hottest atoms — the tail of the velocity distribution — escape from the trap. Basically this is the same idea as blowing on a hot cup of tea in order to cool it. The remaining atoms then re-thermalize in collisions until they follow a thermal velocity distribution again, only now with a lower mean velocity and thus temperature. If we make sure that we lower the trap slowly enough for the atoms to re-thermalize we can cool the atomic cloud without loosing too many atoms. Here high elastic collision rates are advantageous. For this we need distinguishable fermions in two states in the trap and the magnetic offset field tuned to a value where the scattering length is large.

Typically an atomic gas becomes degenerate around $T/T_F \approx 0.5$, today temperatures on the order of $T/T_F \approx 0.1$ can be reached with evaporative cooling.

3.2 Crossed beam traps

In a single beam trap the confinement in axial direction is usually much weaker than in radial direction. This produces highly anisotropic traps which in many cases are not desirable. One way to enhance the confinement in axial direction is to cross two beams with the same waist and power under an angle ϕ with respect to the axial direction z of the single beam. The trapping volume is then given by the intersection of the two beams.

3.2.1 Perpendicular polarization

If the beams are polarized perpendicular to each other as shown in Figure 3.2b the two beams do not interfere in the intersection, the electric fields of the single beams are added quadratically $E_{tot}^2 = E_1^2 + E_2^2$ and the overall intensity is just the sum of the single beam intensities. Hence the trap depth is twice that of the single beam trap:

$$U_0(y) \propto \frac{4P}{\pi w_{0,x} w_{0,y}}. \tag{3.16}$$

Thus, in addition to stronger axial confinement, one gains a factor of two in trap depth, and a factor of $\sqrt{2}$ in trap frequency, by crossing the laser with itself under an angle of 2ϕ and effectively recycling the power in the beam.

3.2.2 Periodic potentials

If the two beams have the same polarization there will be interference effects in the intersection resulting in an intensity modulation with period

$$d = \frac{\lambda}{2 \sin \phi}. \tag{3.17}$$

The trap depth is then given by

$$U_0(y) \propto \frac{8P}{\pi w_{0,x} w_{0,y}} \cos^2\left(\frac{\pi}{d} y\right). \tag{3.18}$$

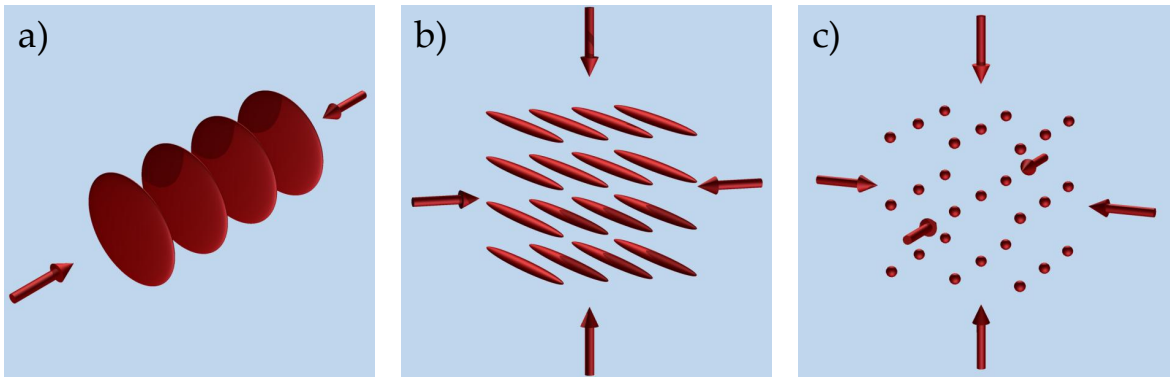

Figure 3.3: Illustration of standing wave traps. a) One retro-reflected beam produces a one-dimensional lattice of pancake shaped traps. b) Two orthogonal standing waves yield a two-dimensional array of one-dimensional tubes. c) A three-dimensional optical lattice with an array of zero-dimensional lattice sites can be realized with three orthogonal standing waves.

which means that the atoms can be trapped in the anti-nodes of this interference pattern. This yields a stack of pancake shaped traps with strong confinement in y-direction as shown in Figure 3.2c. The trap depth in each pancake is four times that of a single beam trap.

Optical lattices

For the special case of $\phi = 90°$, which can be realized by retro-reflecting the laser beam, the interfering electric fields form a standing wave in axial direction. The resulting periodic trapping potential is called an optical lattice with lattice constant $d = \lambda/2$. By superposing two such standing wave traps with perpendicular polarization under an angle of 90° the trapping potential forms a two-dimensional array of one-dimensional tubes. Three orthogonal standing waves form a three-dimensional array of zero-dimensional lattice sites. These kinds of traps are called a one-, two- and three-dimensional lattice, respectively, an illustration of each is shown in Figure 3.3.

3.3 Design criteria for the dipole traps in our experiment

In our experiment we load the atoms from a magneto-optical trap (MOT) into a dipole trap in which we evaporatively cool the atoms to quantum degeneracy. The next step is to transfer the sample into a two-dimensional pancake and finally superpose this with a two-dimensional optical lattice (see Figure 1.1). In the course of this thesis we built the dipole trap for evaporation (which we simply call "the dipole trap") and developed and tested a design for the pancake trap, which will be integrated into the experiment in the near future. In the following we want to present the main considerations which determined the design of these traps.

3.3.1 Dipole trap for evaporation

As the first step on the way to a two-dimensional optical lattice we transfer the atoms from the MOT to a dipole trap for evaporative cooling. In order to make better use of the available beam power and strengthen the confinement in axial direction, this should be a crossed-beam trap with perpendicular polarization of the beams. The beams should travel horizontally and intersect in the horizontal plane as this is easiest to set up. In this orientation the direction of the magnetic offset field used to tune the interactions in the sample is parallel to gravity which simplifies magnetic levitation. The angle of intersection is limited to 6° by the numerical aperture of the viewport of the vacuum chamber (see Figure 4.1).
Since we are working towards a two-dimensional system it is desirable to increase the confinement in one direction with respect to the others in order to make the trap a little flat already. Such a flat trap can be accomplished by making the beam shape elliptical. We want to align the two-dimensional trap horizontally, as optical access for imaging is better from above the experiment chamber. This allows us to image the two-dimensional system with high resolution. Thus the focal waist should be smaller in vertical than in horizontal direction. For reasons of feasibility the aspect ratio was chosen to be approximately 1:5 with waists of $w_{0,\mathrm{vert}} = 20\,\mu\mathrm{m}$ and $w_{0,\mathrm{hor}} = 100\,\mu\mathrm{m}$. The length of the trap is then given by the intersection rather than the Rayleigh range, in our case this is $l = w_{0,\mathrm{hor}} \sin^{-1}\phi = 960\,\mu\mathrm{m}$ while $z_{R,\mathrm{vert}} \approx 1\,\mathrm{mm}$ and $z_{R,\mathrm{hor}} \approx 3\,\mathrm{cm}$. Using a beam with elliptical shape not only provides us with a slightly flatter trap,

it also enhances the confinement along the axial direction. After the transfer into the dipole trap some atoms will be trapped not in the intersection itself, but in the single branches of the intersecting beams. Due to the smaller waist in one direction, corresponding to a shorter Rayleigh range, these atoms will be pulled more strongly into the intersection during evaporation and thus ensure a more efficient cooling cycle.
As mentioned before the laser light for our dipole traps has a wavelength of 1064 nm. In order to realize a trap deep enough to capture the atoms from the MOT ($T \approx 200\,\mu$K, see Section 4.1.3) we use a laser power of 200 W. During the transfer this yields a trap depth of 3.8 mK in the intersection.

3.3.2 Pancake trap

After the sample has been sufficiently cooled in the dipole trap we want to transfer it into a pancake shaped trap which confines the atoms to two dimensions. Such a trapping potential can be realized by loading atoms into one of the interference fringes which appear in a crossed-beam trap with parallel polarization. As explained above we want the pancakes to be aligned horizontally, this means that the beams must cross vertically.
Since we want the pancakes to be as flat as possible we need a large angle of intersection. However, in this we are again limited by the numerical aperture of the vacuum viewport. Hence we choose an angle of $\phi = 7^\circ$. At a laser wavelength of 1064nm this results in a fringe spacing of 4.2 μm (see Equation 3.17).
Now let us estimate the size of the pancakes. The width of the pancake is given by the beam waist $b = 2w_{0,\mathrm{hor}}$ while its length is either given by the Rayleigh range or by the length of the intersection

$$l = \frac{2w_{0,\mathrm{vert}}}{\sin\phi}. \tag{3.19}$$

With an angle of 7° we have $l < z_R$ for beam waists above 5 μm, thus the pancake length is limited by l and amounts to $l \approx 16\, w_{0,\mathrm{vert}}$. In order to give the trap the shape of a round, flat pancake we again need to make the beam shape elliptical. In this case the aspect ratio should be approximately 1:8 to make the pancakes as wide as they are long $b \approx 2 \cdot 8\, w_{0,\mathrm{vert}} \approx l$.
The most important parameter for the pancake trap is the maximum number of atoms

that can be trapped without populating excited trap levels in the strongly confined axis, which would make the trap effectively three-dimensional. Being fermions N identical ^{6}Li atoms will at zero temperature populate the N trap states with lowest energy. If n_i is the number of populated trap levels in direction i and we demand all atoms to be in the ground state in vertical direction ($n_{\mathrm{vert}} = 1$) the total number of populated levels is

$$n = n_{\mathrm{hor}} \cdot n_{\mathrm{ax}}. \tag{3.20}$$

Maximizing this under the condition that the overall energy of each populated state is lower than that of the first excited state in vertical direction

$$\hbar\omega_{\mathrm{hor}}\left(n_{\mathrm{hor}} + \frac{1}{2}\right) + \frac{1}{2}\hbar\omega_{\mathrm{vert}} + \hbar\omega_{\mathrm{ax}}\left(n_{\mathrm{ax}} + \frac{1}{2}\right) < \frac{3}{2}\hbar\omega_{\mathrm{vert}} \tag{3.21}$$

yields $n_{\mathrm{hor}} = \omega_{\mathrm{vert}}/(2\omega_{\mathrm{hor}})$ and $n_{\mathrm{ax}} = \omega_{\mathrm{vert}}/(2\omega_{\mathrm{ax}})$ which means we can trap

$$N = n_{max} = \frac{\omega_{\mathrm{vert}}^2}{4\,\omega_{\mathrm{hor}}\omega_{\mathrm{ax}}} \tag{3.22}$$

atoms per hyperfine state in such a way that the trap is still effectively two-dimensional. This result shows that the dimensionality of the trap does not depend on the absolute values of the trap frequencies but only on their ratio, it is therefore independent of the power in the laser beams. In the experiment we want N to be as large as possible and we choose the beam waists accordingly. We get $N \approx 24\,000$ for $w_{0,\mathrm{vert}} = 75\,\mu$m and thus $w_{0,\mathrm{hor}} = 600\,\mu$m and $l = 1,23\,$mm. At a power of 2 W per beam this yields a trap depth of $U_0 = 6.8\,\mu$K.

Another interesting consideration is how many atoms can be in the dipole trap such that all of them are transferred into only one pancake. This depends on the overlap between the two trapping potentials, i.e. how many atoms in the dipole trap are inside the volume of one pancake. This can be determined by calculating the number of trap levels of the dipole trap in vertical direction $n_{\mathrm{dip,vert}}$ which fit into $y = 2\,\mu$m of space, which is the approximate height of the pancakes:

$$\frac{1}{2}m\omega_{\mathrm{dip,vert}}^2 y^2 = \left(n_{\mathrm{dip,vert}} + \frac{1}{2}\right)\hbar\omega_{\mathrm{dip,vert}} \tag{3.23}$$

where $\omega_{\mathrm{dip,vert}}$ is the trap frequency of the dipole trap in vertical direction. This depends on the power in the dipole trap (via the trap frequency) and yields 900 atoms per hyperfine state for a transfer at $P = 0.25\,\mathrm{W}$, where the dipole trap has a depth of $9.56\,\mu\mathrm{K}$ comparable to that of the pancake trap.
It is not feasible to prepare a dipole trap with so few atoms and we would like to be able to conduct our experiments with more atoms in the pancake. One way around this would be to first make a molecular BEC of the atoms in the dipole trap (see Chapter 5) and then transfer this into the pancake trap. Since the density in a molecular BEC is higher than in a cold thermal gas or a degenerate Fermi gas this would allow us to load more atoms into only one pancake.
Another way to prepare a single two-dimensional trap would be to transfer atoms from a full dipole trap into a stack of pancakes and then empty all but the center pancake. This would load more atoms into the center pancake since atoms in higher excited states in the dipole trap still have a non-zero probability to be in the center of the trap. Emptying the off-center pancakes could be done by driving transitions to one of the states $|4\rangle$-$|6\rangle$ which are then lost from the trap in spin-changing collisions. With the help of a magnetic-field gradient shifting the frequencies of the hyperfine transitions the microwave pulse can be made resonant only outside of the center pancake. At the moment, we are planning to use this method of preparation as it seems to be the most effective and easy way.

4 Experimental Setup

Contents

To trap and cool a gas of atoms to quantum degeneracy a complex experimental apparatus is required. The vacuum chamber in which the experiments take place needs to provide an UHV environment with a pressure $P \leq 10^{-11}$ mbar. Intricate optical setups are used to provide laser light at the appropriate wavelengths and with just the right power and geometry to produce the desired trapping potentials. And finally, strong electromagnets are used to create the required magnetic offset fields. In this chapter we describe the experimental setup needed for every step of the way from a chunk of solid ^{6}Li to a degenerate Fermi gas in two dimensions.

4.1 The starting point

At the beginning of the work for this thesis the group had already assembled the vacuum chamber and succeeded in the preparation of a magneto-optical trap for ^{6}Li. Detailed information on this can be found in the Diploma theses by Martin Ries [Rie10] and Philipp Simon [Sim10], here we will present only the main features of the apparatus they built.

4.1.1 The vacuum chamber

The vacuum chamber consists of an oven chamber and an experiment chamber. In the oven a chunk of solid ^{6}Li is heated to $T \approx 335\,^\circ$C above its melting point at $T \approx 180\,^\circ$C. Hot ^{6}Li atoms emerge through the aperture in front of the oven and

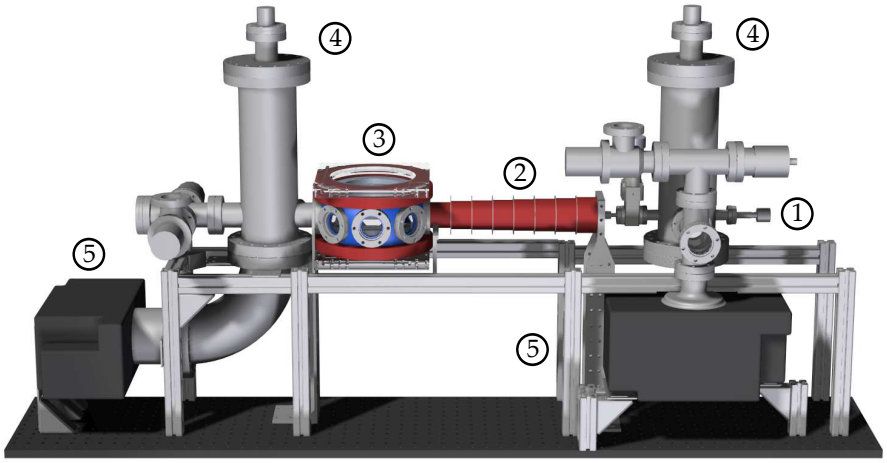

Figure 4.1: Model of the vacuum chamber. The oven (1) is filled with ^{6}Li. When it is heated to $\sim$ 335 °C hot ^{6}Li atoms leave the oven and travel through the Zeeman slower (2) to the heart of the setup, the experiment chamber (3). There they are trapped first in a MOT and later in a succession of dipole traps. The laser light needed to produce the trapping potentials and image the atoms can be shone into the spherical octagon through six viewports on the sides of the octagon and two re-entrant viewports on its top and bottom. The two towers (4) connect the oven and experiment chamber with the ion pumps (5) and serve as gettering surfaces for the titanium sublimators.

travel towards the experiment chamber. The two chambers are connected by a differential pumping stage which also serves as a drift tube for the Zeeman slower. The differential pumping stage allows for ultra-high vacuum in the experiment chamber ($P_{\text{exp}} \approx 10^{-11}$ mbar) whereas the pressure in the oven chamber is slightly higher due to outgassing of the hot oven ($P_{\text{oven}} \approx 3 \cdot 10^{-11}$ mbar). The vacuum is maintained by two ion pumps and two titanium sublimators. The ion pumps are connected to oven and experiment chamber by towers which also serve as gettering surfaces for the titanium sublimators. A three-dimensional model of the vacuum chamber is shown in Figure 4.1.

The heart of the apparatus is the experiment chamber, this is where all experiments take place. The chamber is a spherical octagon with six vacuum viewports on its sides and two re-entrant viewports on top and bottom. These windows are used to shine in the laser light necessary to produce the required trapping potentials and the light for

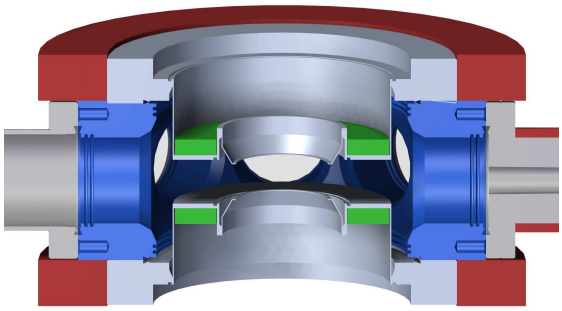

Figure 4.2: Vertical cut through a model of the experimental chamber. The atoms enter the chamber from the right and are trapped in the center of the octagon. The MOT coils (red) are fixed directly onto the octagon, while the coils used to produce strong magnetic offset fields (green) are positioned around the re-entrant viewports so as to be very close to the center of the octagon.

imaging of the atomic cloud. The numerical aperture of the viewports on the sides of the octagon is $\mathrm{NA}_{\mathrm{hor}} = 0.15$ which limits the optical resolution for horizontal imaging to $r = 2.78\,\mu$m. It also restricts the maximum angle of intersection for any crossed-beam dipole traps used in the experiment (see section 3.3). The numerical aperture of the re-entrant viewports is much larger with $\mathrm{NA}_{\mathrm{vert}} = 0.88$, this is possible since they are installed very close to the center of the chamber, as can be seen in Figure 4.2. The re-entrant viewports will later be used to provide optical access for a $\mathrm{NA} = 0.6$ objective with a resolution for vertical imaging at 671nm of $r = 750\,$nm. The objective was designed in our group and is currently being tested (see Friedhelm Serwane's PhD thesis [Ser11]).

4.1.2 The Zeeman slower

When the atoms emerge from the oven they are too fast to be trapped by the magneto-optical trap, hence they need to be slowed down before they reach the MOT. For this purpose a Zeeman slower was installed between oven and experiment chamber. This produces an atomic beam slow enough to be trapped by the MOT which has a maximum capture velocity of approximately 50 m/s.
In a Zeeman slower the atoms are decelerated by the interaction with a laser beam: Every time an atom absorbs a photon it is excited and experiences a recoil of $\hbar k$ in the propagation direction of the photon. After some time the atom relaxes back to

the ground state and emits a photon $\hbar k$ in a random direction. Over many cycles of absorption and emission the net momentum from emission vanishes, whereas the recoil from absorption is always in the same direction and thus adds up. Hence the atom experiences an effective force in the direction of the propagation of the laser light given by

$$\langle \mathbf{F} \rangle = \hbar \mathbf{k} \Gamma_{sc} \tag{4.1}$$

where Γ_{sc} is the scattering rate from Equation 3.15. In order to slow down the atoms most efficiently we need a resonant laser beam counter-propagating with respect to the atomic beam. As the atoms are moving towards the light, the laser has to be red-detuned to compensate for the Doppler shift of the transition. Since the atoms decelerate on their way through the Zeeman slower the detuning needs to be adapted to their current velocity at different positions along the way. This can be achieved by applying a magnetic offset field whose strength decreases along the propagation direction. This induces a Zeeman shift to the atomic resonance frequency and ensures that the atoms are continuously resonant with the counter-propagating laser beam while traveling the length of the Zeeman slower.
The Zeeman slower in our experiment decelerates the atoms from a mean longitudinal velocity of $\bar{v} \approx 1500\,\mathrm{m/s}$ at the oven aperture to approximately $50\,\mathrm{m/s}$ at the center of the experiment chamber. There the atoms are slow enough to be trapped in the MOT [Sim10].

4.1.3 Magneto-optical trap

When the atoms enter the experiment chamber they are confined in space and cooled down by the magneto-optical trap. A MOT is a hybrid trap based on the combination of an inhomogeneous magnetic field and circularly polarized laser beams.
To cool the atoms a MOT exploits the same effect as a Zeeman slower: the net recoil force experienced by an atom when moving towards a red-detuned laser beam. The difference in a MOT is that the laser beams are directed onto the atoms from all six directions (up and down, right and left, back and front). This slows down atomic movement in every direction and thus cools the sample. An atom sitting at rest inside the MOT experiences the same amount of recoil from every beam. However, if an atom has a velocity in a certain direction, the light from that direction is tuned closer

to resonance due to the Doppler shift while the opposite beam is even more red-detuned. Now the recoils from the two beams do not cancel out anymore and a net force acts on the atom and slows it down.

So far this only cools the atoms but does not trap them. To achieve spatial confinement one can exploit the Zeeman splitting of the excited state in an external magnetic field. Installing two coils in an anti-Helmholtz configuration (the distance of the coils is the same as their radius, the currents flow through them in opposite direction) produces a linear magnetic field gradient in all directions:

$$\frac{\mathrm{d}B(x)}{\mathrm{d}x} = \frac{\mathrm{d}B(y)}{\mathrm{d}y} = 2\,\frac{\mathrm{d}B(z)}{\mathrm{d}z} = \text{const.} \tag{4.2}$$

This results in a Zeeman splitting of the excited state proportional to the distance from the center of the trap $z = 0$. At a certain distance r_0 in any direction the detuning of the laser beam shone in from that direction is compensated by the Zeeman shift of the excited state and the transition is resonantly enhanced. Then the net force acting on the atom points in the direction of the beam. In principle every beam fulfills the resonance condition at two points $\pm r_0$, in one case the net force pushes the atom into the trap region, in the other case the atoms would be pushed out of the trap. The latter can be avoided by adjusting the polarization of the laser beams and making use of the selection rule $\Delta m = -1$ for σ^- light and vice versa. An appropriate polarization configuration for a magneto-optical trap is shown in Figure 4.3. From the combination of six circularly polarized laser beams we get a spatially dependent total force which pushes the atoms into the center of the trap from all directions.

Unfortunately with this method atoms cannot be cooled down to $T = 0$, since the absorption of every photon heats the atom by $k_B T = \hbar^2 k^2 / 2m$. The minimum temperature of the sample is reached when the heating rate from absorption equals the cooling rate from the net recoil force. This is called the Doppler limit, it depends on the detuning of the laser Γ, and if the light intensity is small enough to neglect saturation effects it is given by [Fox06]

$$T_D = -\frac{\hbar\Gamma}{2k_B}\,\frac{1 + 4\delta^2/\Gamma^2}{4\delta/\Gamma} \tag{4.3}$$

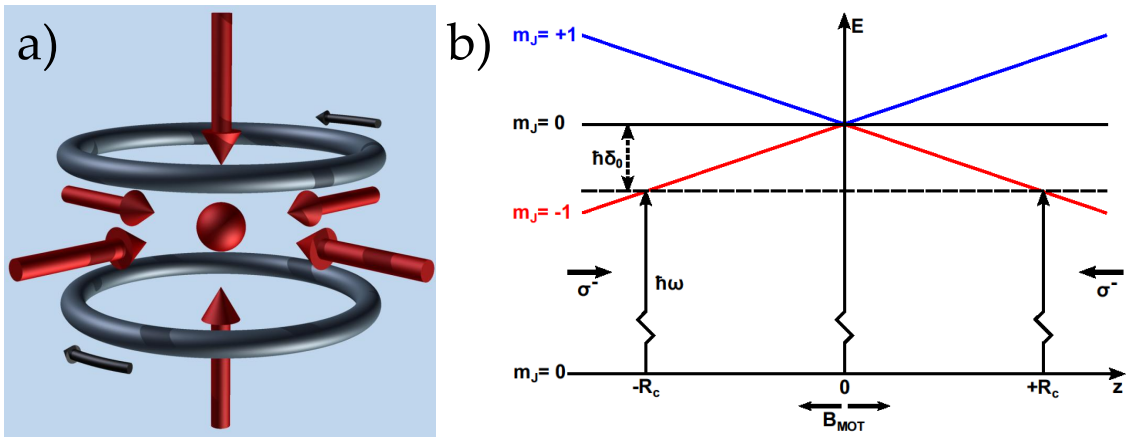

Figure 4.3: a) Illustration of a MOT. Six laser beams and two coils in anti-Helmholtz configuration produce spatial confinement in all directions and cool the atoms to the Doppler limit. b) Working principle of a MOT. The laser with frequency $\hbar\omega$ is resonant with the atomic transition at the distance $\pm r_0$ from the center. At the center the magnetic field changes sign and with it the quantization axis of the atoms. Due to the polarization of the light the beams can only interact with the atoms on one side of the MOT (at r_0 or $-r_0$). With the correct polarization configuration the net force on the atoms always points toward the center of the MOT.

where Γ is the linewidth (FWHM) of the excited state and δ the detuning of the light. The Doppler temperature has a minimum for $\delta = -\Gamma/2$ and in this case we have for ^{6}Li $T_D = 137.6\,\mu$K.

The magneto-optical trap in our experiment consists of two water-cooled coils providing the magnetic field gradient and three laser beams which are red-detuned by 40 MHz from the atomic transition at approximately 671 nm (see Section 2.4.1). The laser light for Zeeman slower and MOT is produced by a TA PRO system (TOPTICA) which consists of a grating stabilized diode laser and a tapered amplifier providing approximately 350 mW of laser power with a linewidth of less than 1 MHz. The frequency of the laser is stabilized by a beat offset lock to a frequency reference. The latter is obtained from Doppler free frequency-modulation spectroscopy of Li vapor [Ser07]. The Zeeman slower light and all three MOT beams are prepared on a separate optical table, where acousto-optical modulators (AOM, CRYSTAL TECHNOLOGY 30100-125 and 3080-125) allow to adjust the power of the beams. The light is coupled into polarization maintaining single-mode optical fibers which transport it

to the experimental apparatus [Rie10]. Fiber couplers placed in front of the vacuum windows of the octagon point the MOT light into the experiment chamber, on the opposite side the light passes a $\lambda/4$-waveplate and is retro-reflected back through the chamber by a mirror (see Figure 4.5). Passing the waveplate twice ensures that the polarization of the beam is flipped on its way back.

Since ^{6}Li is not a simple two-level system an excited atom does not always relax back to the same state and in that case needs to be excited again in order not to lose it from the cooling cycle (see Figure 2.5). Thus the laser light consists of two parts with slightly different detuning called cooler and repumper. The beams have a $1/e^2$ diameter of 11 mm and are made up of three parts cooler and two parts repumper with a total power of approximately 22 mW after the optical fiber. With a current of 34 A flowing through the coils we achieve a magnetic-field gradient of $\mathrm{d}B/\mathrm{d}z \approx 30\,\mathrm{G/cm}$. This configuration produces a magneto-optical trap with a loading rate of $3 \cdot 10^8$ atoms/s at an oven temperature of approximately 350 °C which means that in only one second we can load as many atoms into the MOT as we need for our experiments. Thanks to the ultra-high vacuum in the experiment chamber ($P_{\mathrm{exp}} \approx 10^{-11}$ mbar) the MOT has a vacuum lifetime of 23 min which is much longer than any experimental timescale since typical experiment cycles are on the order of 10 s [Rie10]. Figure 4.4 shows a photograph of our MOT.

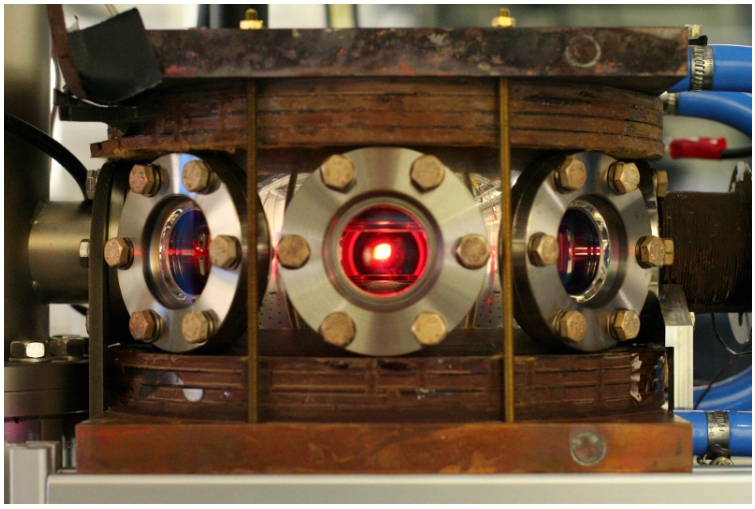

Figure 4.4: Photograph of the MOT in our experiment.

4.1.4 Imaging setup

In order to conduct experiments with our system we need a way to image the atomic cloud inside the experiment chamber. For this we use near-resonant light from a DL PRO diode laser (TOPTICA) which emits approximately 15mW of power. An AOM (CRYSTAL TECHNOLOGY 3080-125) is used to adjust the power of the imaging light and as a fast switch to create short light pulses. The imaging light is split into two parts and coupled into optical fibers. The fiber couplers at the experiment emit collimated imaging beams. One of those is pointed through the experimental chamber horizontally for imaging of the atoms from the side, the other one is coupled out of the fiber above the re-entrant viewport on top of the octagon to provide a second imaging axis. On the other side of the experiment chamber the imaging light is directed onto CCD cameras. With this technique we can take fluorescence as well as absorption images of the atomic cloud in two axes. More information on the imaging setup can be found in [Rie10]

4.1.5 RF setup

Since we want to conduct experiments with three-component Fermi gases of ^{6}Li we need to drive transitions between the three lowest hyperfine states with the help of radio frequency (rf) signals (see Figure 2.6). For this purpose we installed a single loop rf coil inside the experiment chamber. Compared to installing the antenna outside of the chamber, the main advantage of the rf coil inside the vacuum is that it can be placed closer to the atoms and optimally oriented with respect to their position. This allows for stronger rf fields in the trapping region and thus for more efficient transitions between the hyperfine states. Recently, a bachelor thesis has been completed in our group which was concerned with optimizing the rf driving signal to maximum efficiency at the transition frequencies between the states [Heu11].

4.2 The dipole trap

After cooling down the atoms to $\sim 200\,\mu$K in the MOT we transfer them into the dipole trap where we cool the system to degeneracy ($\sim 100\,$nK). Our dipole trap is a far red-detuned crossed-beam trap where the power in the trapping beam is recycled

by directing the beam through the chamber twice under an angle of 6° with respect to the symmetry axis of the octagon.
We use a diode pumped single-mode, linearly polarized continuous-wave Ytterbium fiber laser (IPG Photonics YLR-200-LP) with a rather broad wavelength range of several nanometers around a center of 1068 nm. The laser has a maximum output power of 200 W at an initial $1/e^2$ beam diameter of approximately 2.6 mm.

4.2.1 Optical setup

To produce a dipole trap of the required dimensions the laser beam needs to be shaped appropriately to yield a focus of 20 μm $\times$ 100 μm at the position of the MOT inside the experiment chamber. We will now present the optical setup built for this purpose, a sketch of the beam path is shown in Figure 4.5.
The outcoupler of the fiber laser emits a collimated beam with a diameter of approximately 2.6 mm and linear polarization. We mount the coupler in such a way that the polarization axis is in horizontal direction. First the beam waist is reduced to approximately 500 μm to fit through the aperture of two acousto-optical modulators, one of which is mounted horizontally, the other vertically. We align the AOMs for maximum deflection efficiency into the first order ($\sim$ 80 % overall) and use this for the dipole trap. By changing the power of the radio frequency signal driving the AOMs we can decrease the deflection efficiency and thus stabilize and control the intensity of the trapping light, i.e. the depth of the optical trap. The combination of two perpendicularly mounted AOMs allows a two-dimensional deflection of the beam. This can be used to create a larger, more homogeneous trap by changing the driving frequency of the AOMs, and thus the deflection angle of the beam, fast enough that the atoms experience a time-averaged intensity distribution and trapping potential. In the future this could be used to further flatten the trap to simplify the loading of a single pancake.
Behind the AOMs all light but the (1,1) deflection order is dumped onto a water-cooled beam dump. This is necessary since up to 40 W are dumped here during most of one experiment cycle.
In the next step the beam waist is increased as required to produce the right focal waists with the final $f = 300$ mm focusing lens. To obtain a 1 : 5 elliptical beam

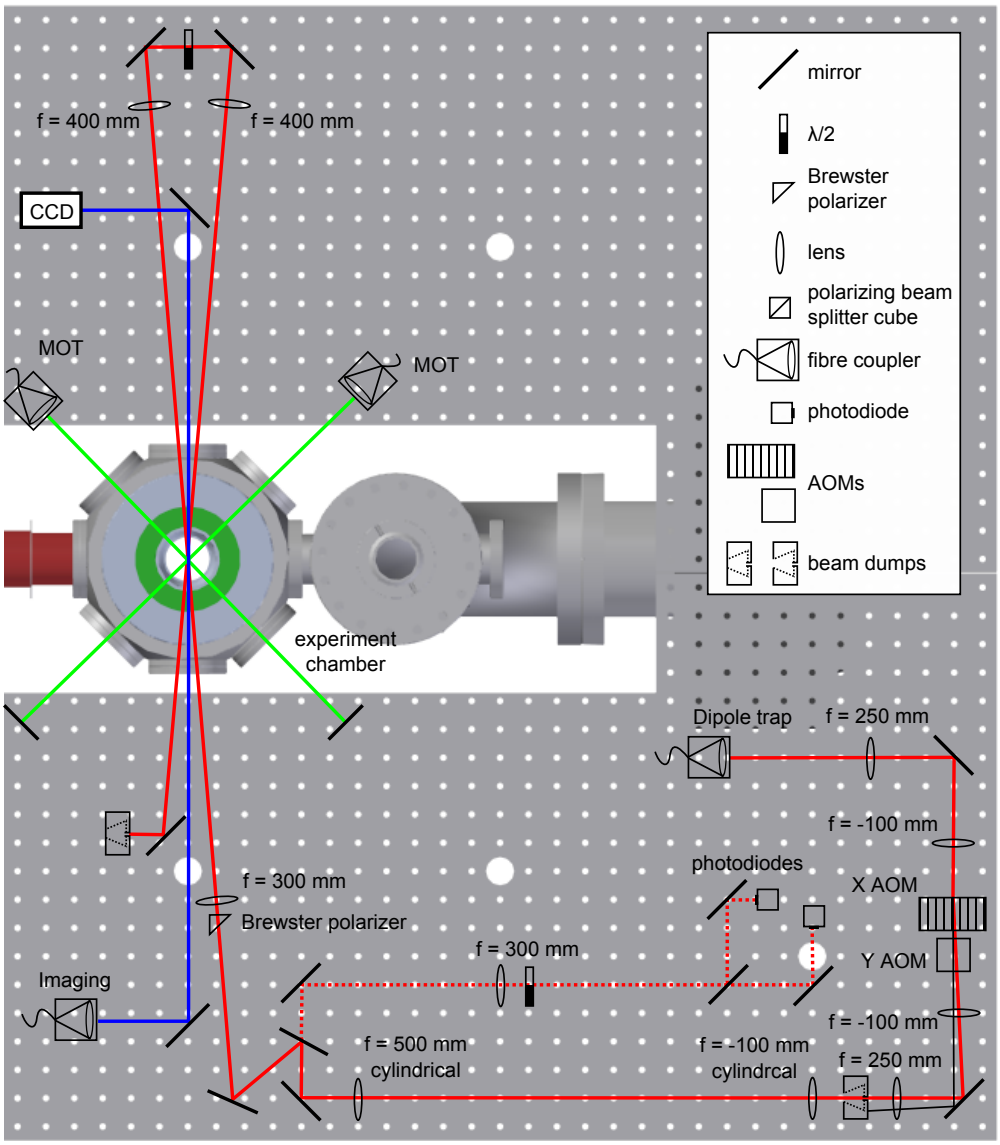

Figure 4.5: Beam path for the optical dipole trap. In the background a sketch of the optical table around the experimental apparatus is shown, on which the optical setup is installed. The dipole trap beam (red) is passed through two AOMs, deflecting the beam in horizontal and vertical direction, which are used for manipulating the power in the beam. Then the beam is given its elliptical shape with a telescope of cylindrical lenses and focused into the experiment chamber under an angle of 6°. On the other side of the octagon the polarization is turned by 90° and focused back through the chamber to create a crossed-beam dipole trap. The dashed red line represents the small part of the beam transmitted by the mirror which is focused onto two photodiodes in order to monitor the power in the beam. The blue line represents the horizontal imaging beam, the green lines are two of the three MOT beams.

we then pass it through a telescope of cylindrical lenses which increases the beam waist in one direction while leaving the other unchanged. Just before the last lens which focuses the beam into the experiment chamber, a Brewster polarizer cleans the polarization to avoid interference effects at the intersection.

The focused beam enters the octagon under an angle of 6° with respect to its symmetry axis. Here we took care to overlap the cross-section of the beam with the MOT. The beam emerges on the far side where an $f = 400\,\text{mm}$ lens collimates it again. Then a $\lambda/2$-waveplate turns the polarization by 90° so as to avoid interference in the crossed beam trap and finally another $f = 400\,\text{mm}$ lens directs the beam back through the chamber. The beam crosses with itself in the center of the experiment chamber at the position of the MOT under a total angle of 12° and is finally dumped on another water-cooled beam dump after emerging from the octagon.

For the preparation of a degenerate Fermi gas and during experiments we need to vary the depth of the optical dipole trap. During transfer from the MOT the laser runs at its maximum power of 200 W. After the transfer this is quickly ramped down to about 40 W which is the minimum power at which the laser runs stable. A further reduction of the intensity of the trapping beam is done with the AOMs in the beam path. By gradually decreasing the rf signal strength we can tune the deflection efficiency and thus the intensity of the trapping beam. This tuning of the rf signal strength is stabilized with a feedback loop: We use the small amount of light transmitted by a mirror ($\leq 0.01\,\%$) and focus it onto two photodiodes to detect any change in power in the trapping beam (dashed red line in Figure 4.5). One of the photodiodes is optimized for the detection of high laser power signals ($\sim 3 - 40\,\text{W}$ in the main trapping beam), the other one for low power signals ($\sim 0 - 3\,\text{W}$ in the main trapping beam). Their response is evaluated by the experiment control system in a PID loop. A signal of 1 V on the high power photodiode corresponds to a trapping beam of 4.06 W, for the low power photodiode 1 V corresponds to a beam power of 350 mW. The photodiode setup allows us to tune the intensity of the trapping beam in a quick and controlled manner.

Figure 4.6 shows a photograph of the complete optical setup for the dipole trap.

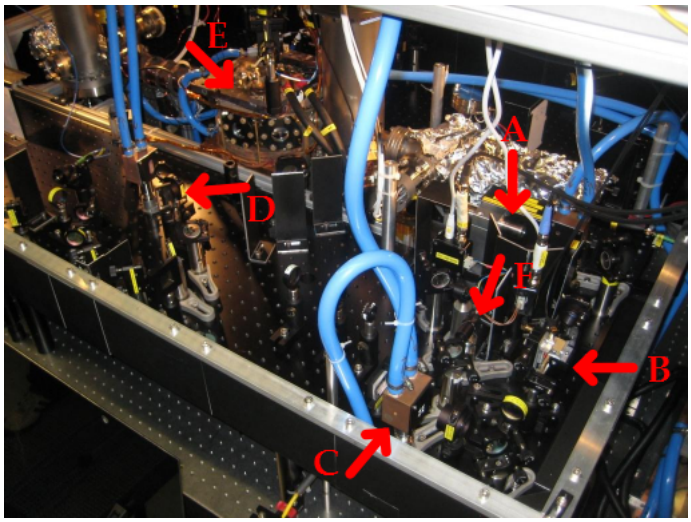

Figure 4.6: Photograph of the optical setup for the dipole trap. The arrows mark the outcoupler for the dipole trap light (A), the AOMs (B) and a water-cooled beam dump (C). To the left of this is the cylindrical telescope. The Brewster polarizer and the final focusing lens (D) can be seen on the left in front of the octagon (E). The photodiode setup (F) is between the beam dump and the outcoupler.

4.2.2 Magnetic offset fields

To control the scattering length inside the atomic cloud we need a homogeneous magnetic field across the trapping region with a magnetic field strength on the order of 1 000 G. Such a field can be produced by two coils in or near Helmholtz configuration, where the distance of the coils equals their radius. In order to achieve strong fields one can either use large coils installed far away or small coils close to the atoms. To reduce the strength of the current and the number of windings required to produce a certain magnetic field at the position of the atoms we decided to mount the coils in the space between the re-entrant viewports and the octagon which is as close to the atoms as possible (1.44 cm, see Figure 4.2). Since space is rather limited at this position we need to use a very compact design for the coils. To enable fast magnetic field ramps during the experiment cycle the coils should have a small inductance.
The magnetic field coils are made from 30 windings of copper wire isolated with capton with a total cross section of $7\,x\,0.6\,\mathrm{mm}^2$. The overall diameter of the coils is 9.29 cm. During experiments currents of up to 200 A have to flow through these coils, which requires very effective cooling. Hence the coils are glued onto a water-cooled

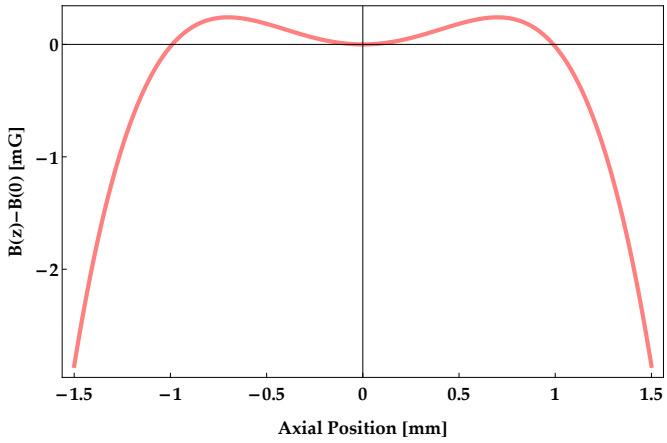

Figure 4.7: Simulation of the magnetic field component in axial direction of the coils depending on the vertical coordinate. The coils are slightly farther apart than in Helmholtz configuration creating an anti-trapping saddle (atoms are in high-field seeking states) in vertical direction. The field in the horizontal plane has a weakly trapping magnetic potential.

copper heat sinks. The combination of strong currents and small coils makes the production technically very challenging.

To avoid overheating of the coils during experiments we installed an interlock system which measures the resistance of the coils in short time intervals and turns off the power supply if the resistance becomes too large. The interlock is adjusted such that the coils cannot become hotter than approximately 75 °C

Before the coils were installed in the experiment they were thoroughly tested. We measured the temperature at the bottom of the coil depending on the current strength using an infrared thermometer (VOLTCRAFT IR-1001A). Additionally we checked for how long high currents can flow through the coils before the interlock shuts down the power supply. Currents of 200 A can continuously flow for approximately 4 s which is long enough for all experimental cycles.

The coils are not mounted in an exact Helmholtz configuration but slightly farther apart. This produces a magnetic field saddle and hence a weak anti-trapping potential in vertical direction and a trapping potential in the horizontal plane. This is desirable as it strengthens the confinement in the axis of weakest optical confinement (axial to laser beams). The desired magnetic field strength in the vertical direction $B(z)$ is shown in Figure 4.7, around the center the x and y dependence of the field is

given by $-1/2B(z)$. This results in horizontal trap frequencies of up to 10 Hz. Unfortunately, one of the coils originally installed in the experiment did not have the desired 30, but only 29 windings. Thus the magnetic field was not as required, but had a gradient across the center of the trap instead of a saddle shape. This was detected during the experiments presented in this thesis and has since been mended by installing a new coil.

4.2.3 Characterization of the dipole trap

Before directing the beam through the experiment chamber we took a picture of the focus produced by the last lens before the octagon. The picture was taken with a beam profiler camera (DataRay, WinCamD) and is shown in Figure 4.8.

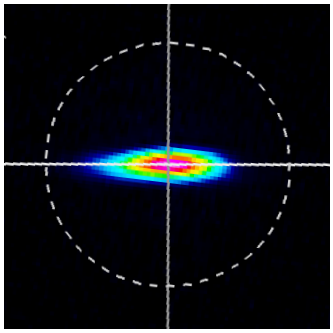

Figure 4.8: Elliptical focus produced by the final $f = 300$ lens before the experiment chamber.

The beam profiler software (DataRay) automatically fits the two axes of the beam with a Gaussian distribution. The waists obtained from this fit are $w_{0,\mathrm{vert}} = 22.4\,\mu$m and $w_{0,\mathrm{hor}} = 79.6\,\mu$m. This yields an aspect ratio of $1 : 3.6$ which is slightly smaller than the desired ratio of $1 : 5$. Since the trap is given by the intersection of two beams and not directly by this focus, this can be only a first estimate of the aspect ratio of the actual trap. A reliable measure of this should be obtained from measurements of the trap frequencies. These will be presented in the following.

Trap frequencies

To measure the confinement which the optical dipole trap imposes on the atomic cloud we excite a collective motion of the cloud inside the trap. From Equation 3.13

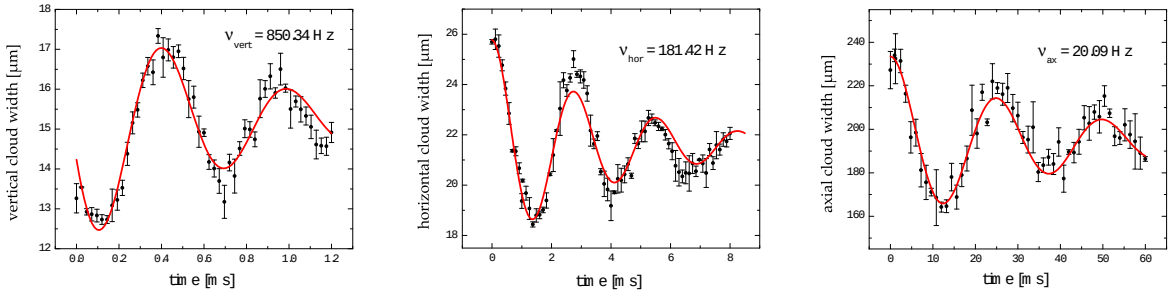

Figure 4.9: Measurement of the trap frequency at a certain trap depth (1 V low power control voltage $\approx$ 350 mW) in vertical, horizontal and axial direction. The fit to the data is a damped sine function, the errorbars are the statistical error of multiple measurements.

we know that the dipole potential looks harmonic in the center of the trap and the associated trap frequency scales with the square root of the beam power (Equation 3.14).

In this experiment we load the optical dipole trap and evaporatively cool the atoms by decreasing the trap depth to a certain value. Then we quickly ramp the magnetic field to $B \approx 523\,\mathrm{G}$, which is close to the zero-crossing of the scattering length, where the atoms do not interact, and suddenly make the dipole trap twice as deep. This excites a collective motion of the atoms in the trap, where the width of the atomic cloud oscillates with twice the trap frequency. The atomic cloud is allowed to follow its collective motion for a certain amount of time before we turn off the trap entirely and take an in-situ image of the cloud. Now we evaluate the width of a Gaussian fit to the cloud shape for different times and fit the oscillation with a damped sine function. Half of the fitted frequency equals the trap frequency. We observe a damping of the signal which is probably due to a dephasing of the collective motion. This might be caused by collisions of the atoms with each other if the magnetic field is not tuned perfectly to the zero-crossing of the scattering length.

By doing one experiment imaging the cloud from the side and one from above, we can evaluate the frequency of the breathing motion in all three directions and thus get a measure for the trap frequency in all three trap axes. In Figure 4.9 we show the results for one value of the trap depth. Surprisingly, the measured trap frequencies are a factor of two smaller than expected.

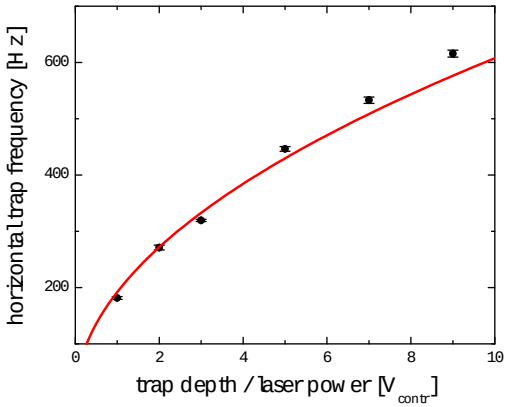

Figure 4.10: Plot of the horizontal trap frequency of the dipole trap measured for different values of the final trap depth measured in terms of the control voltage of the low power photodiode. The error bars are the errors from the fits to the individual trap frequency measurements. The red line represents a square root fit to the data according to $\omega_i \propto \sqrt{P}$.

From these results we can also calculate the anisotropy of the trap. For the trap depth shown in Figure 4.9 we get an aspect ratio $\omega_{\mathrm{ax}} : \omega_{\mathrm{hor}} : \omega_{\mathrm{vert}}$ of $1 : 9 : 42$. The planned aspect ratio of the waists and the length of the trap (Section 3.3.1) is $w_{0,\mathrm{vert}} : w_{0,\mathrm{hor}} : l = 1 : 5 : 48$. Since the trap frequency is inversely proportional to the beam waist (Equation 3.14) we expect an aspect ratio for the trap frequencies of $1 : 9.6 : 48$. Our measurement agrees with this expectation reasonably well, which means that the dipole trap indeed has the desired ellipiticity.

By doing this measurement of the trap frequencies in all three axes for different values of the trap depth we can further characterize the dipole trap. In Figure 4.10 we plot this together with a square root fit to the data according to $\omega_i \propto \sqrt{P}$ (see Equation 3.14). Since the trapping due to the slightly inhomogeneous magnetic offset field is negligible compared to the optical trap frequencies we fixed $\omega_{\mathrm{hor}}(P = 0) = 0$. The fit matches the data reasonably well, discrepancies could be due to the anharmonicity of the trap. Thus it seems that the trap frequencies are systematically too small by a factor of two. This could be explained if the focal beam waists were each a factor of $\sqrt{2}$ larger than planned.

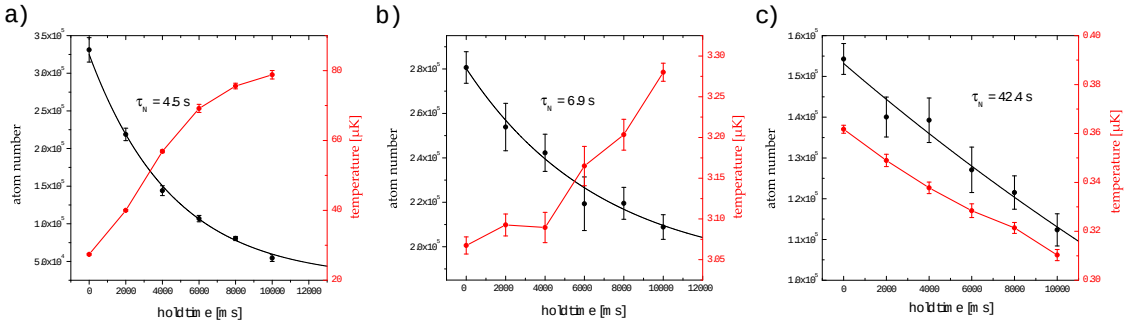

Figure 4.11: Measurement of the change in temperature and atom number over time for three values of the laser power, i. e. trap depth: a) $P \approx 28.4\,\mathrm{W}$, b) $P \approx 2.66\,\mathrm{W}$ and c) $P \approx 350\,\mathrm{mW}$. The change in atom number can be fitted by an exponential decay function with time constant τ.

Lifetime measurements

To make sure that the dipole trap is working correctly we had a closer look at the evaporation. We measured the lifetime and temperature of the atoms in the trap at three points during and after evaporation by ramping to the desired trap depth and there monitoring atom number and temperature over a time of ten seconds. During evaporation the magnetic offset field was chosen such that molecule formation was suppressed. After evaporation, while the cloud was held in the trap, we chose a magnetic offset field of $B \approx 526\,\mathrm{G}$ close to the zero-crossing of the scattering length. There interactions between the atoms in the trap are suppressed. The results of these measurements are shown in Figure 4.11 for three values of the final laser power $P \approx$ 28.4, 2.66 and 0.35 mW. Using the trap frequencies measured in the last section this corresponds to a trap depth of $U_0 \approx 600$, 50 and 6 μK, respectively.

We see that the loss of atoms over time can be fitted by a simple exponential decay function with time constant τ. This tells us that the dominant loss channel is a one-body process, while two- and three body events are negligible. From past experience we know that if the polarization of the two beams is not perfectly perpendicular, strong one-body losses lead to a significantly decreased lifetime of the atoms in the trap [Lom08]. Hence we attribute the short decay time constant at high laser power to a small polarization component parallel in both beams. As the light intensity and thus the trap depth is reduced during evaporation, the lifetime increases. At the end

of evaporation the decay time constant is much larger than the duration of a typical experiment cycle ($\sim 10\,\mathrm{s}$). Hence experiments will not be impeded by loss of atoms from the trap.
In this measurement we also monitored the temperature of the atomic cloud. At the beginning of evaporation heating is quite strong, the temperature rises by 300 % in ten seconds. However, when the gas is cooled further, heating slows down. We attribute this to thermal lensing effects: During transfer from the MOT into the dipole trap, the dipole trap laser runs at a power of 200 W. This causes thermal lensing in the optical setup and shifts the foci of the beams out of the intersection, effectively making the trap more shallow. When the power is ramped down to $P \approx 28.4\,\mathrm{W}$ the thermal lensing effects decrease and the foci move back into the intersection. This makes the trap deeper and compresses the cloud inside the trap which causes heating.
At the end of the evaporation, thermal lensing has stopped and the trap has again the desired depth. In the last measurement at $P \approx 350\,\mathrm{mW}$ the temperature of the sample even seems to go down a little bit with time. However, using Equation 2.11 we can calculate the Fermi temperature and see that we have $T/T_F \approx 0.48$. Thus in this measurement we have prepared a degenerate Fermi gas and we are observing a decrease in the Fermi energy due to particle loss over time rather than an actual decrease in temperature.

4.3 The pancake trap

Once we have cooled down the atoms in the dipole trap we want to transfer them into a two-dimensional potential. To generate this we will use a crossed beam dipole trap with interfering laser beams (see Section 3.3.2). The interference pattern in the intersection of the beams yields a stack of two-dimensional traps for the atoms. In Section 3.3.2 we have explained that the two beams should cross vertically under an angle of 7° and have focal waists of $w_{0,\mathrm{vert}} = 75\,\mu\mathrm{m}$ and $w_{0,\mathrm{hor}} = 600\,\mu\mathrm{m}$ resulting in a pancake length of $l = 1.23\,\mathrm{mm}$
The technical challenge for the setup of the pancake trap lies in the stability of the interference pattern. Since every measurement of any observable in our system is inherently destructive (sending in resonant light for imaging heats up the cloud) we need to be able to prepare the same system under the same conditions many times.

Such reproducibility can only be guaranteed if we load atoms into the same pancake every time, which means the interference pattern is not allowed to drift on the order of fractions of the fringe spacing $d \approx 4\,\mu$m. We estimated that a path difference of the two beams of ~ 10 cm would already result in drifts of the interference pattern on the order of a wavelength, if the atmospheric pressure changed due to normal weather. Hence, as a first measure we decided to make the beam path symmetric for the two intersecting beams.

4.3.1 Optical setup

The simplest way to set up the interferometer is by shaping the beam waists appropriately, splitting the beam into two equally intensive ones with a non-polarizing beam splitter and then using two mirrors to reflect the beams through the experiment chamber under an angle of 7° each. To focus the beams into the center of the octagon we can either use one lens before the beam splitter or two identical lenses after the beam is split in two.

As light source for the pancake trap we will use a NUFERN 50 W fibre amplifier seeded by a low-noise continuous-wave single-frequency 1064 nm laser with an output power of 500 mW (INNOLIGHT Mephisto S 500 NE). To get a sufficiently deep trapping potential in the pancake we will need up to 4 W of power in the beam before it is split up. The rest of the 50 W of power supplied by the NUFERN will be used for the two-dimensional optical lattice. In order to stabilize and regulate the power in the beam we plan to send it through an AOM and use the first deflection order, as we do for the dipole trap. Then we want to couple the light into an optical fibre to clean the beam shape and be able to install the lasers away from the experimental chamber. Since it is difficult to couple a laser with this much intensity into an optical fiber without damaging it, we plan on using polarization maintaining single-mode fibers with high-power connectors (OZ Optics).

After the fiber the beam waists will be shaped as required before the light enters the interferometer. We want the focal beam waists at the intersection to be $w_{0,\mathrm{vert}} = 75\,\mu$m and $w_{0,\mathrm{hor}} = 600\,\mu$m (see Section 3.3.2). One easy way to produce this is by making the beam elliptical and then focusing it with a spherical lens with large focal length before the beam is split in two. Alternatively we could shape the beam to 600 μm

in both directions and use two cylindrical lenses inside the interferometer two focus the vertical waist down to 75 μm. At the moment we plan on using the first method, we have however designed the interferometer such as to allow a change of plans in this respect. Hence we shape the beam appropriately with the fiber outcoupler, then a cylindrical telescope widens the beam vertically with an aspect ratio of approximately $1:8$ and finally a $f = 1000$ mm lens focuses the beam.
In order to build a feedback loop for the AOM used to regulate the light intensity, we will also need to integrate a photodiode setup after the fiber just as we have done in the dipole trap setup.

4.3.2 Stability tests

To get a measure of how stable we can make the pancakes we wanted to monitor the interference pattern in a test setup. As a light source we used a single frequency laser with 1 mW output power at a wavelength of 1064 nm (Lightwave Technology) and coupled this into a fiber. To make things easier we did not shape the beam waists in any way, apart from focusing the beams with two lenses, and decided to install the optical elements horizontally on a breadboard. At the point of intersection we placed a microscope objective with a $\times 40$ magnification and imaged the magnified interference pattern onto a CCD camera (GUPPY F-503) with a pixel size of $2.2 \times 2.2\,\mu\text{m}^2$. A sketch of the optical setup can be found in the inset of Figure 4.13.
First we qualitatively tested the reaction of the interference pattern to different disturbances. We leaned on the optical table, simulated air drafts and temperature changes with a blow dryer and knocked against the mounts of each optical element. From these tests we learned that the interference pattern is generally quite sensitive to such disturbances. The stability of some optical elements however seems to be more crucial for the stability of the interference pattern than others. While any optical element before the beam is split in two (e.g. the fiber coupler) have a rather weak influence on the fringes, the beam splitter seems to be the most sensitive element. This was to be expected since any disturbance before splitting the beams influences both in the same way, while any disturbance at the point of splitting can influence the relative path difference and for example change the angle of intersection. We learned that using pedestal posts (THORLABS 1 inch pedestal pillar posts) instead of normal posts

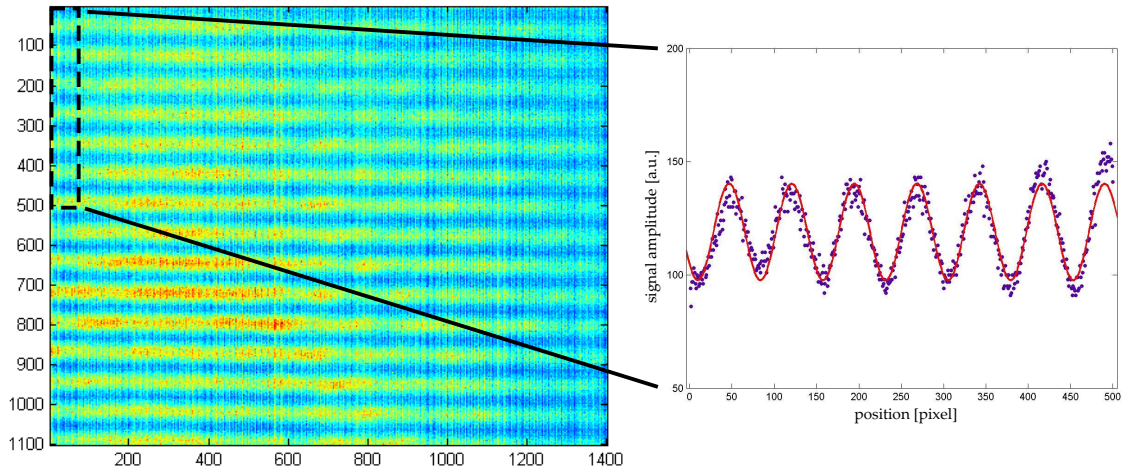

Figure 4.12: A typical image of the interference pattern in the test setup taken with a $\times 40$ microscope objective and a CCD camera is shown on the left. The plot on the right shows the data extracted from the region of interest approximately marked by the dashed box and a fit to the data with a squared sine function.

(THORLABS 1/2 inch optical posts and post holders) increases the robustness of the setup quite significantly with respect to such disturbances as described above.

Finally we wanted to examine the stability of the pancakes over a long period of time without introducing any disturbances on purpose. For this we set the CCD camera to take an image of the interference pattern every minute for more than five days. A typical image taken during this measurement is shown in Figure 4.12. Additionally to the horizontal fringes of the interference pattern we can see an inhomogeneities along the fringes. These were not examined further in this test measurement as they are probably caused by the imaging setup.

We analyzed the fringe pattern with MATLAB. First we cut out a region of interest containing approximately ten fringes and integrated over ten pixels along the fringes to get an average fringe pattern for every image. Then we fitted this with a squared sine function. The frequency of the fits is equivalent to the pancake spacing while the change of the fitted phase over time is a measure of the drift of the interference pattern in space. The fitted values for the phase during the entire measurement are plotted in Figure 4.13.

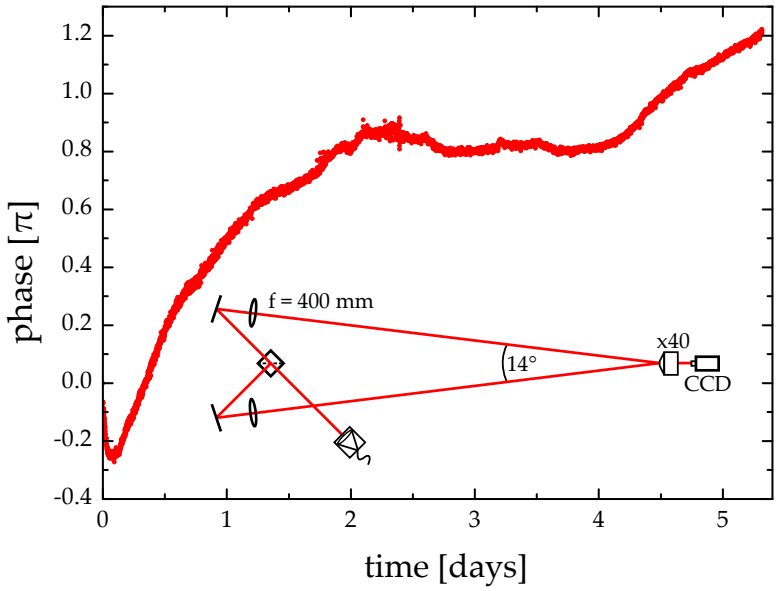

Figure 4.13: Drifts of the interference pattern in the test setup over a period of five days. The inset shows a sketch of the optical setup we used for this experiment.

The data shows shot-to-shot fluctuations of approximately $1/20\,\pi$ which is equal to 5 % of the pancake spacing. We think that this would be acceptable in the experiment. However, we can also see a slow drift of the pattern over π, or equivalently one pancake spacing, in the first two days. After that the pattern stays relatively stable for two more days before it starts to drift again. Since the range of this slow drift is as large as an entire pancake spacing this would limit the reproducibility of our experiments, as we could not be sure if we were loading atoms into the same pancake in every experiment cycle. One way to overcome this would be to actively stabilize the pattern by monitoring it during experiments and slightly correct the beam path if necessary. This would be possible since the large, problematic drifts are very slow while fast shot-to-shot fluctuations are small.

From this test measurement we cannot be sure that all of the observed are in fact caused by drifts in the interference pattern, the imaging setup could contribute to the instabilities as well. Nevertheless we decided to design a special apparatus for the optics of the interferometer which offers improved stability on both short and long timescales.

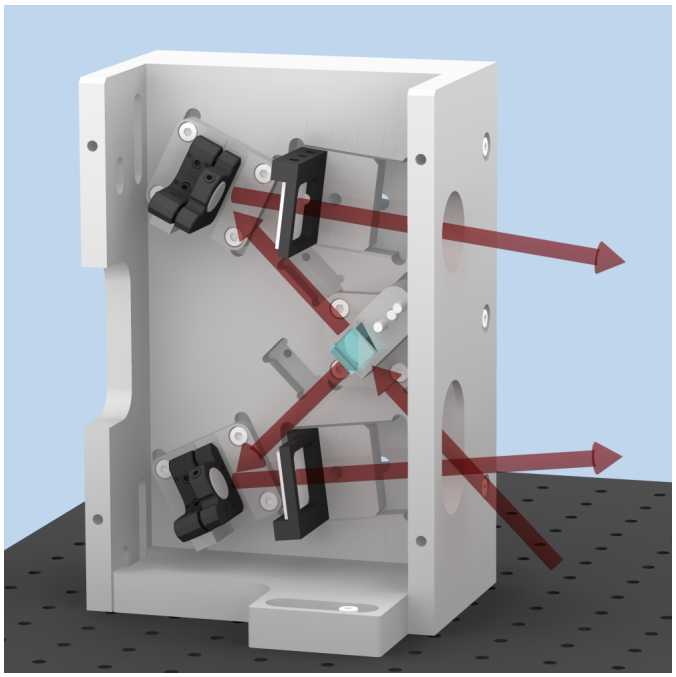

Figure 4.14: Three-dimensional model of the final design for the casing of the interferometer. In the experiment the casing will be closed off with a lid and all aluminum parts will be anodized.

4.3.3 Design of a compact interferometer casing

Our goal was to build a compact, closed and very stable casing in which the optical elements necessary to produce two focused, vertically intersecting beams (beam splitter, mirrors and lenses) can be installed in correct alignment with each other, and which itself can be fixed onto the optical table in front of the experiment chamber.

At first we tried to design a solid aluminum frame with very precise cut-outs into which the optical elements could be fixed with screws. However, during the design we found that this would be impossible to engineer to the required precision, even more so considering that we expected — from practical experience — that things could change from the initial plan in the actual implementation. Hence we decided to go for a more modular, variable design where we would have the possibility to change single components of the apparatus without having to build a new one from scratch. Nevertheless, the final design was still quite intricate and challenging to build. A three-dimensional model is shown in Figure 4.14.

In the final design for the casing the beam enters the apparatus under and angle of 45° with respect to the horizontal plane. Inside it is split up by a 50 : 50 non-polarizing beam splitter cube (Edmund Optics). The two beams are reflected off two 1/2 inch mirror mounts (THORLABS KS05 1/2" Precision Kinematic Mirror Mount) with an angle of 7° to the horizontal plane each. Optionally we can install two cylindrical lenses in the beam path after the mirrors to produce the right focus at the intersection. As can be seen in Figure 4.14 all optical components are fixed onto aluminum mounts which in turn are precisely fitted into the massive aluminum main piece of the casing. This leaves us the freedom to change single components, e.g. use a beam splitting plate instead of a cube which would need a different mount. Additionally we included more space along the beam path for the mounts of the cylindrical lenses to be able to adjust the focus as needed. For higher alignment precision we asked the workshop to engrave scales along the cut-outs.
The front plate of the casing has two holes where the beam enters and the two beams emerge. The back plate also has a clearance, this was included since at this position a mirror of the dipole trap optics would be in the way of the interferometer. The main piece, front and back plate are screwed and doweled onto the base plate which can be fixed onto the optical table with screws through elongated holes. This allows to align the entire casing with respect to the experimental chamber. Finally an aluminum lid closes off the casing. In order to be able to make fine adjustments to the alignment of the mirrors after the casing has been closed, we put holes into the casing in the right positions to reach all set and lock screws of the mirror mounts with an Allen key.
Figure 4.15 shows a photograph of the completed apparatus. When this picture was taken we were testing whether we could shape the beams as required and align everything as planned before having all aluminum parts anodized black. Overall the design worked as planned, however two small adjustments were made: We needed an additional mirror in front of the casing to correctly direct the beam into the casing. For this we fixed one 45° mirror mount (THORLABS H45B2 45° Optic Mount) directly onto the front plate of the apparatus and used a custom-made mirror mount to then point the beam 45° upwards. Since such a large casing takes up a large amount of space in front of the experimental chamber where space is limited, we decided to fix another 45° mirror mount directly onto the front plate at the height of the atoms inside the chamber (10 cm above the optical table) which we can later use to direct

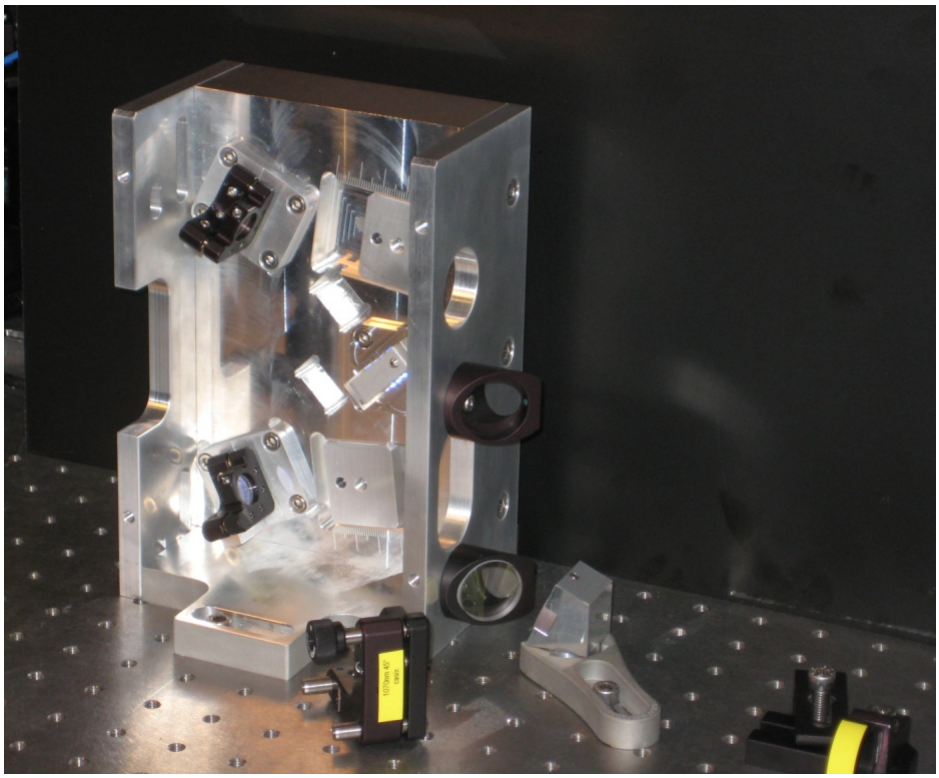

Figure 4.15: Photograph of the completed interferometer without the lid and before being anodized. In front of the casing some optical elements of the beam path on a height of 25 mm above the optical table can be seen. The not yet anodized aluminum mirror mount was custom-made to produce the 45° angle of the beam when entering the apparatus.

the imaging light for the horizontal imaging axes into the octagon.
Now the casing has been anodized and a new test setup has been built, this time including the entire beam path needed to shape the correct focal waists. In this setup we can thoroughly test the stability and homogeneity of the interference pattern we can produce with this interferometer. The results of these measurements will be published in a Bachelor thesis [Sta12].

5 Preparation of a molecular BEC

Contents

One of the first experiments performed with the new dipole trap was to prepare a molecular Bose-Einstein condensate (mBEC) of ^{6}Li atoms. By evaporatively cooling the trapped atomic cloud it was possible to observe a molecular BEC. We could thus verify that we are indeed able to cool down the atoms to degeneracy with our setup. In the following we will briefly explain the observed experimental signature of a BEC, a bimodal density distribution after time-of-flight. Then we will describe the experimental procedure we used and finally present our first molecular BEC and discuss the experimental results.

5.1 Properties of the mBEC

We evaporatively cool a mixture of ^{6}Li atoms in states $|1\rangle$ and $|2\rangle$ while the homogeneous magnetic offset field is set to 786 G, which is just below the Feshbach resonance of the two states. Here the atoms are strongly interacting, which is favorable for efficient evaporation since thermalization due to collisions is fast. As the scattering length is positive, the interaction potential supports a bound state and the atoms can form $|12\rangle$ molecules.

As the polarizability of the molecules is twice that of the atoms, at the same laser power the trap is twice as deep for molecules. During evaporation this effect suppresses the loss of molecules compared to the loss of atoms. If the trap depth is lowered slowly enough for the cloud to thermalize the ratio of molecule to atom number

reaches an equilibrium which depends on the temperature of the cloud [Chi04]:

$$\frac{N_{\mathrm{mol}}}{N_{\mathrm{at}}} = \phi_{\mathrm{at}} e^{E_B/k_B T} \tag{5.1}$$

where ϕ_{at} is the phase-space density of the atoms E_B is the binding energy of the molecules. When the thermal energy of the gas is comparable to the molecular binding energy (Equation 2.32)

$$k_B T \sim \frac{\hbar^2}{ma^2} \quad \xrightarrow{^6\mathrm{Li}} \quad T \approx 750\mathrm{nK} \tag{5.2}$$

molecules are accumulated in the trap and the atomic gas of fermions becomes a gas of bosonic molecules. When these composite bosons are cooled down even more at a critical temperature T_c (Equation 2.5) they form a Bose-Einstein condensate.

Above the transition temperature the gas forms a thermal cloud. At low temperatures the bosonic nature of the molecules has to be taken into account when calculating the density of the thermal gas. It is determined by the Bose function $g_{3/2}(x) = \sum_i x^i / i^{3/2}$ instead of a Maxwell-Boltzmann distribution [Ket99]:

$$n_{\mathrm{th}}(\mathbf{r}) = \frac{1}{\lambda_T} g_{3/2}\left(e^{(\mu - V(\mathbf{r}))/k_B T}\right). \tag{5.3}$$

In the analysis we will use a Gaussian distribution instead, which is a good approximation at least for hight temperature.

When the trap is turned off the cloud expands according to the particles' momenta and the interaction energy is transformed into kinetic energy in the expansion. We can calculate the temperature of the thermal cloud from the width of the distribution after time-of-flight t as

$$w_{\mathrm{th}} = \sqrt{w_0^2 + \frac{k_B T}{m} t^2}. \tag{5.4}$$

We estimate the initial width w_0 of the cloud inside our trap from in-situ absorption images to be approximately $10 - 15\,\mu$m. For a sufficiently long time-of-flight w_0 can be neglected. At a typical temperature of 100 nK the second term in the equation dominates over the first one after a time-of-flight of 1ms. In this experiment we took absorption images of the cloud after a time-of-flight of $t = 5$ ms. Thus neglecting

w_0 in the calculation of the temperature works well for our measurements at higher temperature, but introduces some inaccuracy for the lowest two data points.

Below the critical temperature the molecules condense into a Bose-Einstein condensate. To find the density distribution of a BEC of interacting particles one has to solve the time-independent Gross-Pitaevskii equation [Pet02]:

$$\left(\frac{\hat{p}^2}{2m} + V_{\text{ext}}(\mathbf{r}) + g|\Psi(\mathbf{r},t)|^2\right)\Psi(\mathbf{r}) = \mu\Psi(\mathbf{r}) \tag{5.5}$$

with the chemical potential μ. This is a non-linear Schrödinger equation with a mean-field interaction term depending only on the density and the mean-field interaction $g\delta(\mathbf{r}-\mathbf{r}_0)$ where $g = 4\pi\hbar^2 a/m$. This mean-field interaction energy density is the same as in Equation 2.30 and can only be used to describe the system if $na^3 \ll 1$.

Solving Equation 5.5 analytically is hard since it is a nonlinear differential equation. In our system the interaction energy is much larger than the kinetic energy of the particles, thus we can neglect the latter in the so-called Thomas-Fermi approximation. This yields for the spatial density distribution:

$$n_{\text{BEC}}(\mathbf{r}) = |\Psi(\mathbf{r})|^2 = \max\left(\frac{\mu - V_{\text{ext}}(\mathbf{r})}{g}, 0\right). \tag{5.6}$$

Figuratively speaking the condensate fills the bottom of the trap up to the chemical potential. In a harmonic trap the density thus has the shape of an upside-down parabola [Ket99]:

$$n_{\text{BEC}}(\mathbf{r}) = \frac{15N}{8\pi\bar{R}^3}\max\left(1 - \sum_{i=1}^{3}\frac{x_i^2}{R_i^2}, 0\right). \tag{5.7}$$

Here $R_i = 2\mu/m\omega_i^2$ is the Thomas-Fermi radius with $\bar{R} = (R_x R_y R_z)^{1/3}$. At the Thomas-Fermi radius the wavefunction of the BEC goes to zero, it is thus a measure of the size of the condensate.

As we have said above, neglecting the particles' kinetic energy to use the Thomas-Fermi approximation is justified in our case. However, interactions might even be so strong that $na^3 \ll 1$ is no longer true. This means that the Gross-Pitaevskii equation does not necessarily apply to our system. Nevertheless, we can use Equation 5.7 as a first approximation in the analysis of our data.

When the cloud is released from the trap for a time-of-flight measurement, it expands as interaction energy is converted into kinetic energy. The stronger the interaction in the gas, the faster the expansion. This expansion simply rescales the parabolic shape of the cloud [Ket99]. In an anisotropic trap, expansion is fastest in the direction of strongest confinement, in a time-of-flight image a cloud released from such a trap thus inverts its aspect ratio during expansion.
In a harmonic trap not all of the molecules condense at the same time. When we cool the trapped cloud the molecules in the center of the trap condense first while particles farther out are still in the normal phase. The condensate fraction grows with decreasing temperature. When the trap is turned off both the condensed and thermal part of the cloud expand in their typical shape of a parabola and an approximate Gaussian, respectively. Observing a bimodal density distribution of an upside-down parabola with Gaussian wings in time-of-flight measurements would be clear experimental evidence of a molecular BEC.

5.2 Experiment Sequence

Now that we know what to look for to find the mBEC — a bimodal density distribution — let us briefly explain the experimental procedure we used to observe this. A timing graph of the most important steps is shown in Figure 5.1.
The first step in the experiment is to load the MOT from the atomic beam entering the experiment chamber. After a loading time of one second we have enough atoms in the MOT for the experiment ($\sim 10^8$). We turn off the Zeeman slower and prepare the MOT for the transfer of the atoms into the dipole trap.
To get optimal starting conditions for evaporation in the dipole trap we want the MOT to be very cold and dense. We can achieve this by ramping the detuning of the cooler and repumper light closer to resonance. A detuning of $\delta = -\Gamma/2$ yields the minimum temperature with maximum confinement (see Equation 4.3). As a smaller detuning leads to increased photon scattering, we need to lower the power in the MOT beams at the same time. Here the intensity of the repumper is lowered more slowly than that of the cooler to allow the repumper to transfer more atoms out of the states $|3\rangle - |6\rangle$ such that the atoms are accumulated in states $|1\rangle$ and $|2\rangle$. This yields the desired $|1\rangle$-$|2\rangle$-mixture in the trap.

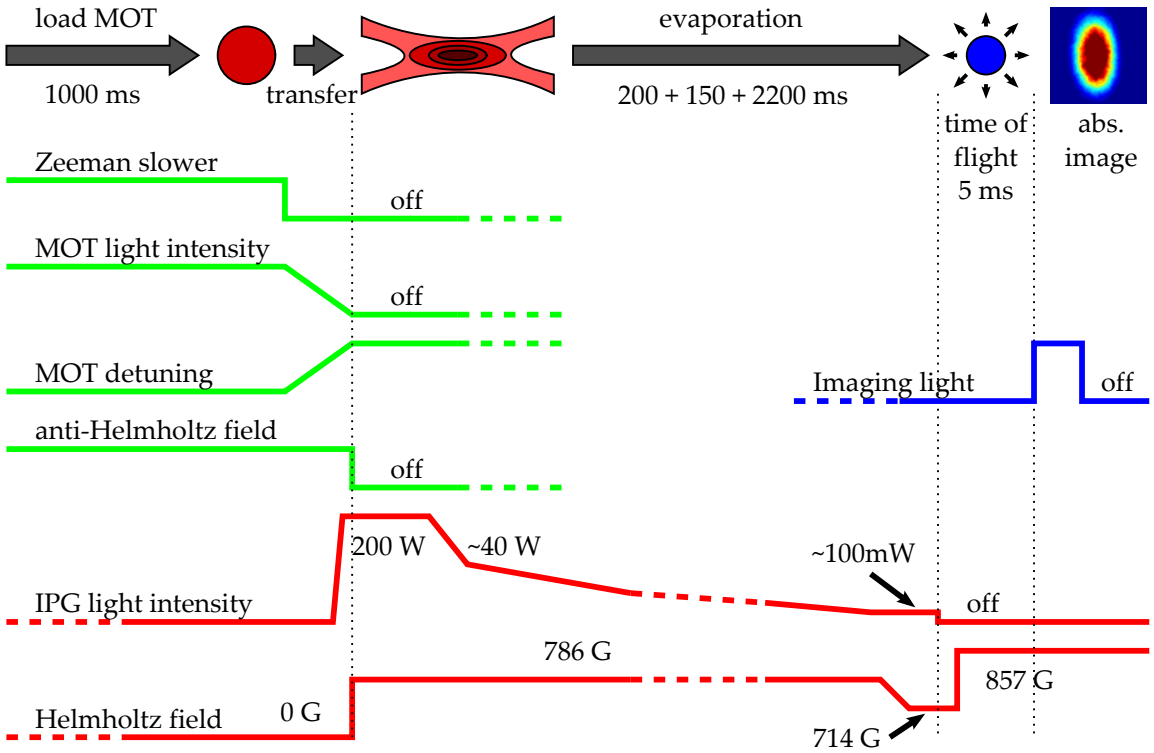

Figure 5.1: Illustrative timing graph of the experimental procedure to produce and observe a BEC of $^6Li_2$ molecules. At the top the main steps in the experiment are shown: loading of the MOT, transfer into the dipole trap, evaporative cooling, time-of-flight expansion and finally absorption imaging of the cloud. Below that each step is explained in more detail. The green lines explain the laser light and magnetic fields for the MOT, red ones show the dipole trap light and the Feshbach field, the blue line represents the imaging light. Times and amplitudes are not to scale.

Right before the transfer we turn on the laser for the dipole trap and tune it to its maximum power of 200 W. Then we turn off the anti-Helmholtz field and the light for the MOT and switch on the magnetic offset field. Now we have trapped approximately 10^6 atoms in the intersection of the dipole trap with a Helmholtz field of 786 G. At this magnetic field value the $|1\rangle$-$|2\rangle$-mixture of atoms has a large positive scattering length of about $7\,000\,a_0$ (see Figure 2.7). This is a strongly interacting gas which is necessary for efficient evaporative cooling.
We leave the dipole trap laser running on high power for 200 ms of plain evaporation during which the hottest atoms escape from the trap. Afterwards we ramp down the power of the laser to approximately 40 W in 150 ms to avoid thermal lensing effects of the optical elements. Then we lower the intensity of the trapping beam even more with the help of the two AOMs in the beam path (see Section 4.2.1). We drive two linear ramps to cool down the sample. The first ramp goes from 40 W to $\sim 3\,W$ in one second, the second one takes the intensity in 1200 ms from there to the desired final trap depth on the order of 100 mW. The timings for the evaporation sequence have been optimized for a maximum ratio of atom number to temperature at the end of the evaporation.
After the evaporation and before the cloud is released from the trap we ramp the magnetic offset field to a lower value of 714 G where the scattering length is approximately a third of its former value with $a \approx 2\,000\,a_0$. This is done in order to better observe the bimodal density distribution: The thermal cloud expands according to its temperature while the condensate expands as interaction energy is turned into kinetic energy. Thus for a smaller scattering length the condensate expands more slowly resulting in a stronger separation of the two phases making the observation of the typical bimodal shape easier. After the magnetic field ramp the cloud is released from the trap by switching off the dipole trap laser entirely.
After one millisecond of time-of-flight most of the interaction energy of the condensate should have been transformed into kinetic energy. Now the molecular BEC expands with a constant velocity and we can tune the magnetic field to a different value again.
In order to image both the thermal and condensed part of the cloud at the same time we need to dissolve the molecules into atoms again. We can do this by ramping the magnetic field across the Feshbach resonance, to a value where the scattering

length is negative and no molecular state exists. Here we chose $B = 857\,\mathrm{G}$ with $a \approx -20\,000\,a_0$. After 5ms of time-of-flight we take an absorption image by shining the resonant imaging light onto the cloud for a short time ($10\,\mu\mathrm{s}$) and imaging the transmission onto a CCD camera. For this experiment we use the vertical imaging axis. Comparing this with a reference (no atoms) and a background picture (no atoms, no imaging light), taken in quick succession after the actual absorption picture, yields the density of the cloud integrated along the imaging axis.
Imaging destroys the sample, as photon scattering causes heating and for the next measurement we have to repeat the experiment cycle again.

5.3 Results and Analysis

We performed the measurement explained above several times for different values of the final trap depth. For the analysis we took the average of 159 images for each value of the final trap depth. Then we integrated the images along the y-direction and analysed the resulting one-dimensional, twice-integrated distribution. The two-dimensional images and the twice-integrated data can be seen in Figure 5.2, it shows the condensation of the cloud as the trap depth, and thus the temperature, is lowered. We fitted the data with a bimodal fit of a Gaussian for the thermal wings and the square of an upside-down parabola for the condensate. The fitted function is

$$f(x) = A_{\mathrm{th}} \exp\left(-\frac{(x-x_0)^2}{2w_{\mathrm{th}}^2}\right) + A_c \left(1 - \frac{(x-x_0)^2}{w_c^2}\right)^2 \tag{5.8}$$

where the fit parameters are the width of the thermal cloud w_{th} and the BEC w_c, respectively, and the center x_0 of the distribution. The square to the condensate density is due to the integration along the imaging and y axes. Integrating the density of the thermal cloud twice yields a Gaussian function again. The amplitudes of the Gaussian and the squared parabola contain the remaining fit parameters

$$A_{\mathrm{th}} = \frac{1-f_c}{\sqrt{2\pi}w_{\mathrm{th}}} A_{\mathrm{tot}} \tag{5.9}$$

$$A_c = \frac{15}{16 w_c} f_c\, A_{\mathrm{tot}} \tag{5.10}$$

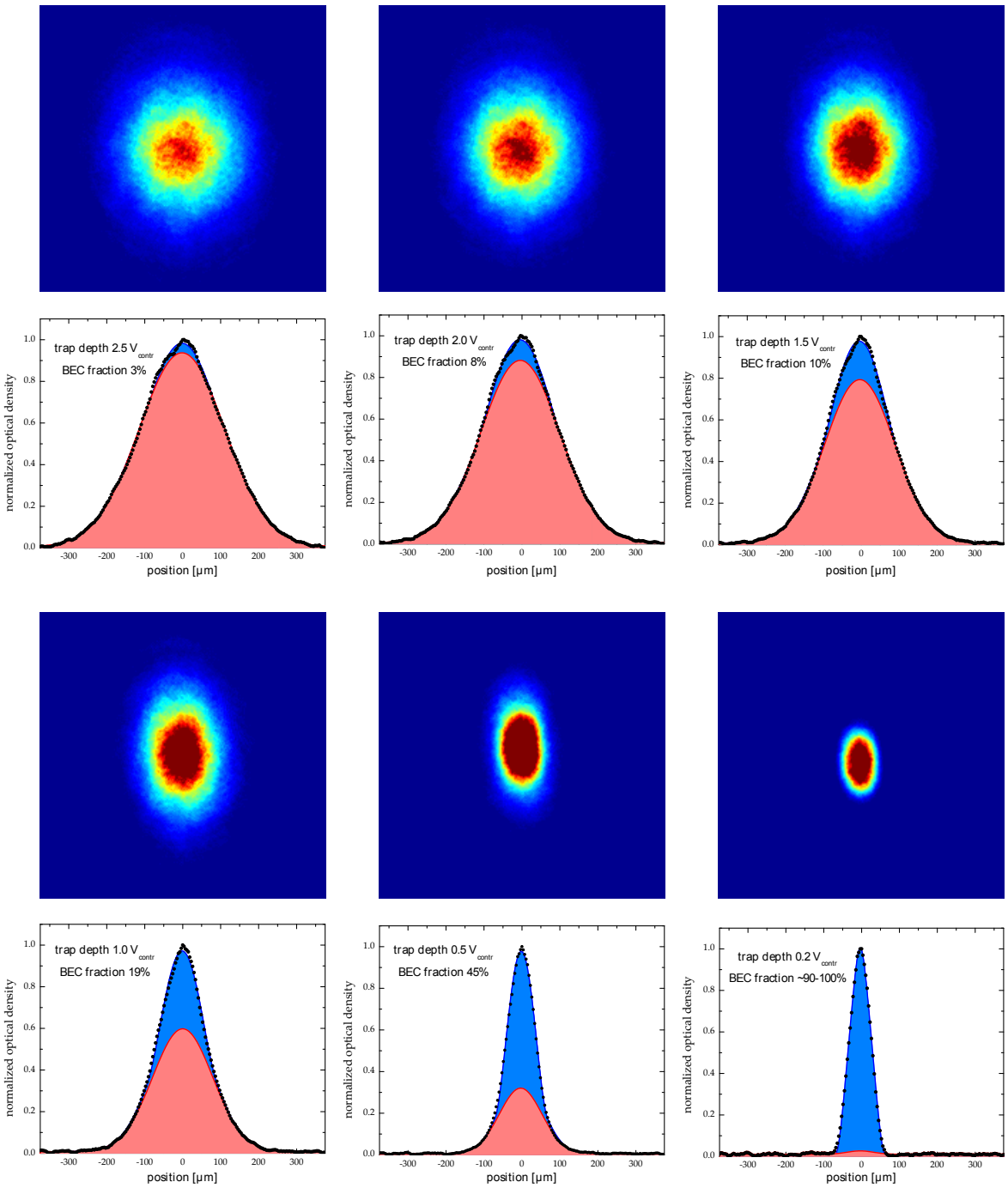

Figure 5.2: Averaged false-color absorption images of the sample after 5ms of time-of-flight together with the twice-integrated normalized density distribution obtained from the images (black data points). For decreasing final trap depth the bimodal shape of the cloud becomes apparent as a kink in the density distribution. The red curve is a Gaussian fit to the wings of the distribution, the blue shaded area shows the deviation of the bimodal distribution (blue curve) from the Gaussian.

with the condensate fraction $f_c = N_0/N$ and the total area defined by $A_{\text{tot}} = \int f(x)\mathrm{d}x$. As expected the cloud changes its shape during evaporation from a thermal gas with a Gaussian density distribution at high trap depth to an almost completely condensed cloud with parabolic shape at the lowest value of the trap depth. During the condensation the bimodal distribution emerges as a kink in the twice-integrated density ditribution (see Figure 5.2).

Setting up the bimodal distribution as a simple sum of condensate and thermal distribution neglects interaction effects: In truth, the condensate pushes the thermal part of the cloud out of the center of the trap. However, a bimodal fit including these effects would involve coupled equations for the two parts and be very hard to solve.

In Table 5.1 the condensate fraction and width of the thermal cloud obtained from the fits are listed according to the final trap depth. From these parameters together with the trap frequencies measured in experiments as in section 4.2.3 we can calculate the actual and the critical temperature for each trap depth. Also, by integrating over the twice-integrated density distribution one more time we can estimate the atom number in state $|1\rangle$ for each measurement.

The signal the CCD camera measures in an absorption image is the optical column density n_{opt} in the direction of the imaging beam. This is related to the total number of atoms in the sample by the pixel area of the camera A, the magnification of the imaging setup M and the resonant absorption cross section of the atoms σ_0:

$$N = \frac{A}{M^2\,\sigma_0} \sum_{x,y} n_{\text{opt}}. \tag{5.11}$$

We estimate that the magnification is unity to an accuracy of 10 %, this leads to a relative error in the atom number of 20 %. Since the imaging light is only resonant with one transition, by changing the detuning we can image atoms in state $|1\rangle$, $|2\rangle$ or $|3\rangle$ but never more than one state at the same time. In this experiment we should have an approximately balanced mixture of atoms in states $|1\rangle$ and $|2\rangle$. The total number of atoms in the sample should thus be roughly a factor of two of the number obtained from the measurement via Equation 5.11.

The atom number in state $|1\rangle$ obtained from the data is shown in Table 5.1. The coldest cloud, which is an almost pure condensate, contains approximately 25 000 atoms

trap depth $[V_{\text{contr}}]$	$N_{\|1\rangle}$	f_c	w_{th} [μm]	$\bar{\omega}[Hz]$	T [nK]	T_c [nK]	T/T_c
0.2	$24\,672 \pm 4\,934$	$\sim 0.9 - 1$	–	441.0 ± 11.2	–	92.2 ± 6.6	–
0.5	$61\,277 \pm 12\,255$	0.45 ± 0.05	53.5 ± 2.7	695.7 ± 17.6	82.9 ± 8.3	196.9 ± 14.0	0.42 ± 0.05
1.0	$87\,823 \pm 17\,564$	0.19 ± 0.02	77.5 ± 3.9	986.7 ± 25.0	174.0 ± 17.4	314.9 ± 22.5	0.55 ± 0.07
1.5	$964\,847 \pm 19\,369$	0.1 ± 0.01	91.9 ± 4.6	$1\,207.6 \pm 30.6$	244.7 ± 24.5	398.2 ± 28.4	0.61 ± 0.08
2.0	$100\,009 \pm 20\,001$	0.08 ± 0.02	106.6 ± 5.4	$1\,394.8 \pm 35.3$	329.0 ± 32.9	464.8 ± 33.1	0.71 ± 0.09
2.5	$102\,017 \pm 20\,403$	0.03 ± 0.03	114.9 ± 5.7	$1\,559.6 \pm 39.5$	382.6 ± 38.3	523.2 ± 37.3	0.73 ± 0.09

Table 5.1: Results of the bimodal fit to the twice-integrated density distribution measured for different final trap depths in units of the control voltage. For the lowest trap depth a Gaussian fit to the thermal wings was not possible since the sample was almost completely condensed and no thermal cloud was discernible. The atom number is obtained from integrating over the density distribution and the average trap frequency is calculated from the trap frequency measurements in section 4.2.3.

in each state. This would just be sufficient to load the two-dimensional trap, which cannot hold more than 24 000 atoms in two dimensions (see Section 3.3.2). However, it should be possible to improve on this number quite significantly. We think that the number of atoms in the condensate will increase now that we have installed the new coil for the magnetic offset field. Also, we could improve the efficiency of evaporation by lowering the trap depth following an optimized formula [Luo06] instead of driving simple linear ramps.

The temperature of the sample can be obtained from the width of the Gaussian fit to the thermal wings of the twice-integrated density distribution using Equation 5.4 with $w_0 \approx 0$. The critical temperature for the sample in each measurement follows from Equation 2.5. As input parameters we use the atom numbers from above and the trap frequencies obtained from the measurements described in section 4.2.3. It was not possible to fit thermal wings to the twice-integrated density at the lowest trap depth since the cloud was almost completely condensed in this measurement. Nonetheless, we can at least say that T/T_c in this measurement should be between zero and T/T_c for the next higher trap depth where we could still fit a Gaussian to the thermal wings.

Since our sample is far from non-interacting ($a \approx 2\,000\,a_0$) we do not expect the equations introduced in section 2.1 to describe our system. However, finding a correct theoretical description for a strongly-interacting molecular BEC is much too difficult for our purposes. We only want to characterize evaporative cooling in our new dipole trap and show that we can use it to prepare a degenerate quantum gas. For this we compare our results to Equation 2.8. Re-written in terms of our fitting parameters this reads

$$f_c = \left(1 - \left(\frac{T}{T_c^0}\right)^3\right). \tag{5.12}$$

Here T_c^0 is the critical temperature for condensation in a non-interacting gas, for which this equation holds true. In Figure 5.3 we have plotted Equation 5.12 as well as the condensate fractions obtained from our measurements over T/T_c^0.

Clearly, and as was to be expected, our data does not match this theory. This can be the case due to a number of reasons. One of them is that we probably do not have a perfectly balanced mixture of states $|1\rangle$ and $|2\rangle$ in the sample. Atoms without a

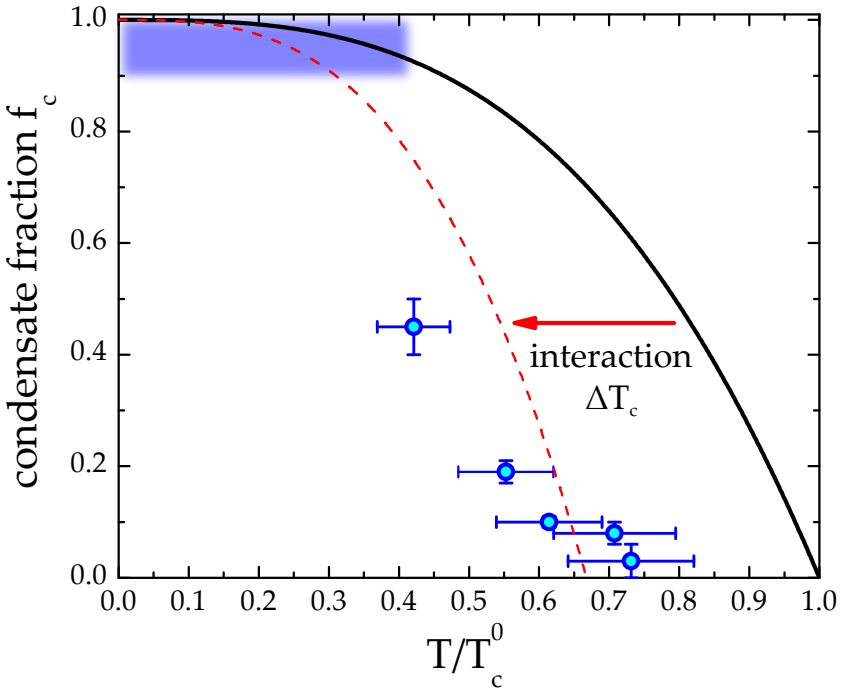

Figure 5.3: Condensate fraction over T/T_c^0 for the data taken in our experiment. The data points are obtained from the Gaussian fits to the thermal wings of each sample. The blue shaded area represents the confidence interval we can give for the measurement at the lowest trap depth where we could not fit a temperature. The black line represents Equation 5.12 which is valid for an ideal non-interacting Bose gas. Taking interactions in the gas into account as a shift to the critical temperature for condensation, and fitting this to the data leads to the red dashed line.

"partner" in the other state cannot form a molecule and can thus not condense into the molecular BEC. This would lead to a condensate fraction smaller than expected at higher temperatures. However, once the trap is so far evaporated that the trap depth reaches the chemical potential of the atoms they are lost from the trap while the molecules stay trapped. This allows us to prepare an almost entirely condensed cloud starting from an imbalanced thermal gas.

Much more important is the fact that our molecular BEC is not at all non-interacting which not only limits the reliability of our fit results but also means that Equation 5.12 is simply not applicable to describe our data. Interactions in the system lead to a change in the critical temperature: $T_c = T_c^0 + \Delta T_c$. For a harmonically trapped cold gas this interaction shift of the critical temperature has two contributions. On the

one hand repulsive interactions enhance condensation which leads to a shift of T_c to higher temperatures. On the other hand there is a mean-field effect reducing the critical temperature. This has been studied for example by S. Giorgini, L. P. Pitaevskii and S. Stringari [Gio96]. Their research determined the overall ΔT_c including both effects to be negative.
More recent research in the group of Z. Hadzibabic reveals beyond-mean-field effects of critical correlations on T_c [Smi11]. These critical correlations seem to stabilize the condensate and lessening the negative shift. Unfortunately, they were only able to measure the shift in a weakly interacting Bose gases, however we have to assume that our gas of composite bosons is in the strongly interacting regime. Thus, from their data we cannot get an estimate of the ΔT_c in our experiment, however it seems reasonable to expect an overall negative shift of T_c.
Fitting a function of the form

$$f_c = \left(1 - \left(\frac{T}{T_c^0 + \Delta T_c}\right)^3\right) \tag{5.13}$$

to our data yields the red dashed line in Figure 5.3 with $\Delta T_c / T_c^0 = -0.33$. Even if we cannot interpret this quantitatively, it is tending in the right direction. Thus interaction effects seem a plausible explanation for the deviation of our data from the theory valid for ideal Bose gases.

6 Radio frequency spectroscopy of ^{6}Li

Contents

By applying a radio frequency field to the atoms we can drive transitions between different hyperfine substates. As the energy splitting between these states depends on the magnetic offset field, we can use radio frequency spectroscopy to calibrate the magnetic field in our experiment. Most importantly though, we can use it for the controlled preparation of a three-component mixture of ^{6}Li atoms. This is the basis for doing experiments with ultracold three-component Fermi gases, which our experiment is designed for. RF spectroscopy is also an essential tool to probe properties of the sample under study, for example by measuring the binding energy of molecules. In this chapter we will first give a brief summary of the effects of near-resonant light on a two-level system before presenting our rf spectroscopy measurements.

6.1 Rabi oscillations in a two-level system

The states in the two-level model of an atom can be coupled by an electro-magnetic field oscillating at the resonance frequency $\nu = (E_{|e\rangle} - E_{|g\rangle})/h$, where $E_{|g\rangle}$ and $E_{|e\rangle}$ are the energy of the ground and excited state, respectively. This coupling leads to an oscillation between the two states as the oscillating field drives the atom in a cycle of excitation and relaxation processes. In a sample of two-level atoms the occupation probability of the excited state oscillates with half the Rabi frequency [Foo07, Met02]:

$$p_{|e\rangle}(t) = \sin^2\left(\frac{\Omega t}{2}\right) \tag{6.1}$$

if at $t = 0$ all atoms were in the ground state, i.e. $p_{|e\rangle}(0) = 0$.
In our experiment we usually want to transfer atoms between the three substates $|1\rangle$, $|2\rangle$ and $|3\rangle$ of the $\{2^2S_{1/2}, m_s = -1/2\}$ ground state. The three states differ in the magnetic quantum number of the nuclear spin m_I, thus driving transitions between them corresponds to flipping the nuclear spin of the atom. The Rabi frequency depends on the strength of the oscillating magnetic field $\mathbf{B}$ as

$$\Omega \propto \mu \mathbf{B}\mathbf{S}. \tag{6.2}$$

Here $\mathbf{S}$ is the spin being flipped and μ its magnetic moment. In our case nuclear and electron spin are not entirely decoupled which means that μ is larger than the nuclear magnetic moment. For the $|1\rangle - |2\rangle$ transition it is $\mu \approx 1/100\,\mu_B$ where μ_B is Bohr's magneton.
The larger the Rabi frequency, the faster it is possible to prepare the atoms in a certain state. Hence to be able to prepare states with a short lifetime we need a large Rabi frequency. Since the amplitude of the oscillating magnetic field depends on the power of the radio frequency signal as $B \propto \sqrt{P}$, the maximum Rabi frequency is limited by the power we can apply and the efficiency with which this is transmitted to the single loop coil. A Bachelor thesis has been written on the optimization of the setup to this end [Heu11].
If the driving frequency is not exactly on resonance, but has a detuning Δ, the Rabi frequency changes. Time-dependent perturbation theory yields [Met02]

$$\Omega_{\text{eff}} = \sqrt{\Omega^2 + \Delta^2} \tag{6.3}$$

$$\text{and} \qquad p_{|e\rangle}(t) = \left(\frac{\Omega}{\Omega_{\text{eff}}}\right)^2 \sin^2\left(\frac{\Omega_{\text{eff}} t}{2}\right). \tag{6.4}$$

The Rabi frequency increases while the maximum occupation in the excited state decreases.

6.2 Driving transitions between states

For this experiment we again prepared the atomic cloud in the crossed beam dipole trap and cooled it down by evaporation. Since we want to transfer free atoms between

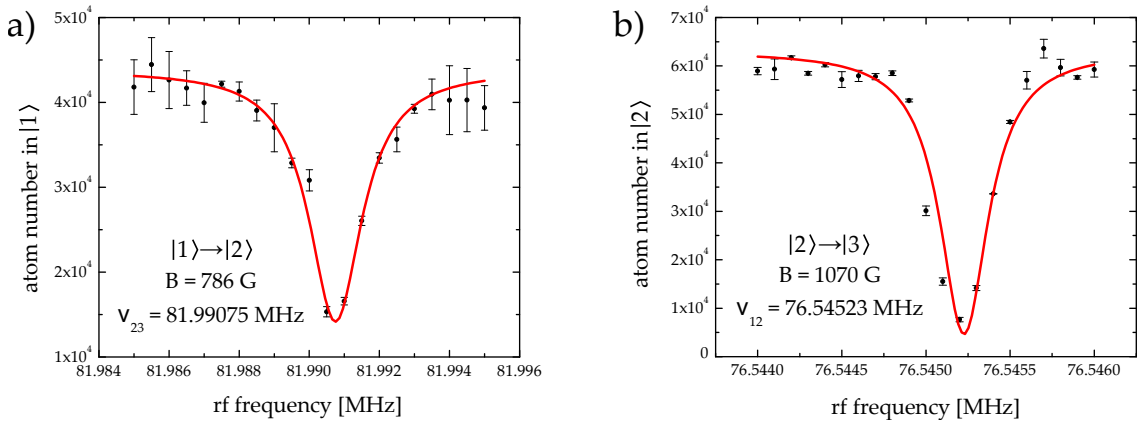

Figure 6.1: Frequency sweeps across the resonance for the transitions a) $|2\rangle - |3\rangle$ and b) $|1\rangle - |2\rangle$. The fit to the data is a Lorentzian, the magnetic offset field was determined from the fitted resonance frequency via the Breit-Rabi equation.

the states we stopped the evaporation before molecules could be accumulated in the gas. To find the resonance frequency of the $|2\rangle - |3\rangle$ transition we applied a 50 ms long radio frequency pulse with a power of 20 mW to the atoms and monitored the remaining atom number in state $|2\rangle$. Scanning the frequency across the resonance we observe a dip in the population of state $|2\rangle$ as atoms are transferred into state $|3\rangle$. Figure 6.1a shows an example of such a measurement. To find the resonance frequency we can fit a Lorentzian to the data. Then we can use the Breit-Rabi formula to calculate the magnetic offset field at which the transition between state $|2\rangle$ and $|3\rangle$ has this frequency. From the data in Figure 6.1a we calibrate the magnetic field to be B=786 G in this measurement.

To find the resonance frequency of the $|1\rangle - |2\rangle$ transition we can do the same measurement. However, to keep the condition $p_{|e\rangle}(0) = 0$, we have to remove all atoms in state $|2\rangle$ before applying the rf pulse. This can be achieved by exposing the sample to imaging light for a short time. If the detuning of the imaging beam is chosen for imaging of state $|2\rangle$, these atoms will absorb the light and consequently be heated up until they are lost from the trap. The atoms in state $|1\rangle$ will not be affected by this as long as the imaging pulse is not too strong. Figure 6.1b shows a measurement of this transition using an rf pulse 2 ms long with a power of 6 mW at a magnetic offset field of 1070 G.

By doing such frequency scans across the resonance for different values of the current

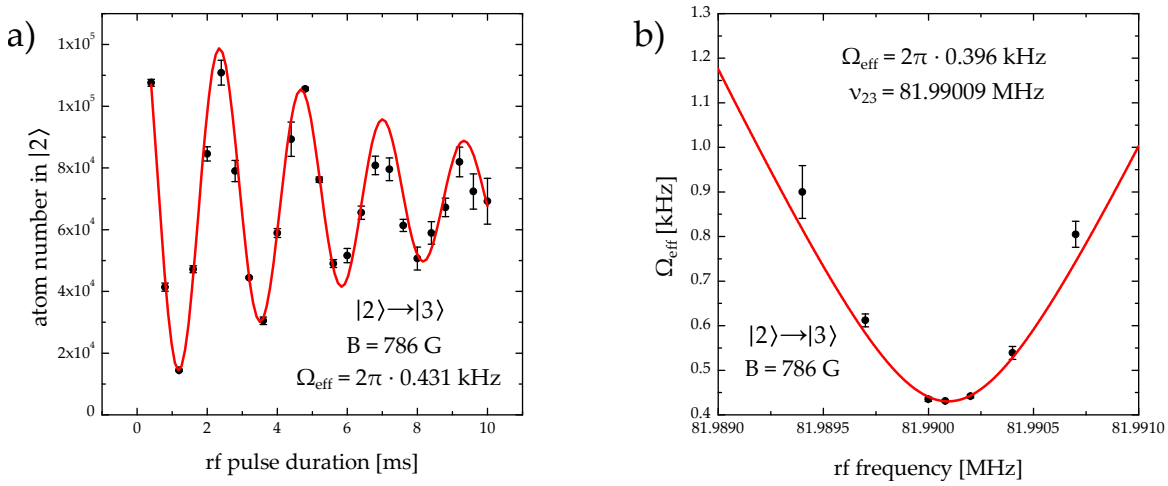

Figure 6.2: a) Rabi oscillation of atoms between state $|2\rangle$ and $|3\rangle$ at a magnetic offset field of 786 G and an rf frequency of 81.99008 MHz. The power of the rf pulse in this measurement was 200 mW. b) Dependence of the effective Rabi frequency on the detuning of the rf pulse.

flowing through the Helmholtz field coils, we can calibrate the magnetic offset field in our experiment.

6.3 Measuring the Rabi frequency

Once we approximately know the resonance frequency of a transition from measurements as presented in the last section we can observe Rabi oscillations of the population in one of the states by varying the length of the rf pulse. Figure 6.2a shows an example of such an experiment for an rf pulse with frequency $\nu = 81.99008$ MHz and a power of 200 mW at $B = 786$ G. We fitted the data with a damped sine function to obtain the effective Rabi frequency. The damping of the oscillation is due to decoherence effects as atoms in different states collide or feel a slightly different magnetic field.

Varying the frequency of the rf signal yields the effective Rabi frequency for the $|2\rangle - |3\rangle$ transition depending on the detuning with respect to resonance. This is plotted for a magnetic offset field of $B = 786$ G in Figure 6.2b together with a fit of Equation 6.3 to the data. From this we get for the resonance frequency at $B = 786$ G $\nu_{23} = 81.99009$ MHz and a Rabi frequency of $\Omega_{23} = 2\pi \cdot 0.396$ kHz.

The experiments presented here were performed by applying an rf pulse of 200 mW to the single loop coil in the vacuum chamber. In the future we want to increase this to 100 W. However, to avoid overheating of the wire inside the vacuum by dissipation of some of the power, which could compromise the ultra-high vacuum, we wanted to implement an interlock system to shut down the rf signal if the vacuum cable gets too hot. During the above measurements the interlock system was still being developed. Thus we only used low power rf signals to eliminate the risk of damaging the experimental setup.
To get an estimate of the Rabi frequencies achievable in the experiment once we can apply high-power pulses, we can scale our result with the square-root of the power. At $P_{\mathrm{rf}} = 100\,W$ this yields $\Omega_{23} = 2\pi \cdot 8.85\,\mathrm{kHz}$. This is slightly larger than the Rabi frequencies measured in the old experiment of $\Omega_{23} = 2\pi \cdot 7\,\mathrm{kHz}$, where the single loop coil was not installed inside the vacuum chamber but at the re-entrant viewport below the chamber. We hoped that by positioning the new single loop coil closer and optimally oriented with respect to the position of the atoms we could achieve larger Rabi frequencies. So far our results look promising, but to verify this we need to do some experiments with the rf setup at full power and directly measure the Rabi frequencies for both transitions $|1\rangle - |2\rangle$ and $|2\rangle - |3\rangle$.

7 Conclusion and outlook

At the beginning of this diploma thesis in March 2011 our group had completed the setup of the vacuum chamber built a magneto-optical trap with fast loading rates and an excellent vacuum lifetime.

During the last year we have further developed the experiment towards its final setup. We have built an optical dipole trap in a crossed-beam configuration using a 200 W Ytterbium fiber laser with a wavelength of 1064 nm and transfered a mixtures of $\sim 10^6$ atoms in two different states from the MOT into the dipole trap. We also installed two coils in approximate Helmholtz configuration around the re-entrant viewports of the experiment chamber with which we can apply strong, homogeneous magnetic offset fields. By changing the amount of current flowing through the coils, and thus the magnetic field in the experiment chamber, we can tune the inter-particle interactions in the Fermi gas.

With this setup we were able to evaporatively cool the two-component atomic mixture down to the Nanokelvin regime where the sample became quantum degenerate. Experimental proof for this was the observation of a molecular Bose-Einstein condensate when the gas was cooled at large values of the scattering length just below the Feshbach resonance. We were able to prepare almost completely condensed clouds of approximately 25 000 atoms per spin state. Here we were limited by a residual magnetic field gradient across the trapping region. The installation of a new Helmholtz field coil should significantly increase the number of atoms in the trap after evaporation.

In the next step we put the radio frequency setup into operation and performed rf spectroscopy on the trapped atomic gas. With these measurements we calibrated the magnetic field in our experiment and got a first estimate of the Rabi frequencies we can achieve with this rf setup.

In the near future we want to test the rf setup with higher power and better determine the Rabi frequencies we can achieve. Then we will prepare a three-component Fermi

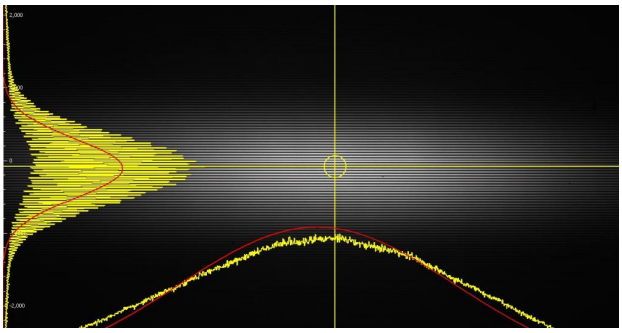

Figure 7.1: $\times$ 7.3 magnified CCD camera image of the interference pattern produced with the custom-made interferometer. The fringes have a distance of 4.95 μm, they are quite flat and homogeneous, no curvature or internal structure is discernible.

gas and do some experiments with it to further test the setup.

While putting the dipole trap into operation we were already working on the next step, developing the setup for the interferometer which will produce the pancake shaped trapping potential for the atoms. Only recently the fiber amplifier, which we will use as the laser light source for the pancake trap, arrived. And by now the tests on our custom-made interferometer concerning the stability and homogeneity of the pancakes have been completed as well. As can be seen in Figure 7.1 there is no discernible structure on the fringes, they look very homogeneous. The pattern has a periodicity of 4.95 μm and is quite stable. Shot-to-shot fluctuations are still on the order of $1/20\,\pi$, but long-term stability has improved significantly with the custom-made interferometer, no drifts larger than $0.6\,\pi$ could be observed during two weeks of continuous observation [Sta12]. The results of these latest test measurements look very promising and we want to integrate the two-dimensional trap setup into the experiment very soon. Then we can transfer the cold atomic gas prepared in the dipole trap into the two-dimensional trap. Developing a technique to empty all but one pancake, or only load a single one to begin with, may take some time. However, we can already do some interesting experiments with a stack of two-dimensional gases, which the imaging process would average over.

The high-resolution objective designed in our group has recently arrived as well and can be installed above the experiment chamber very soon. The objective has a resolution of 750 nm over a field of view of $\varnothing 200\,\mu$m and will be used to image the two-dimensional cloud from above.

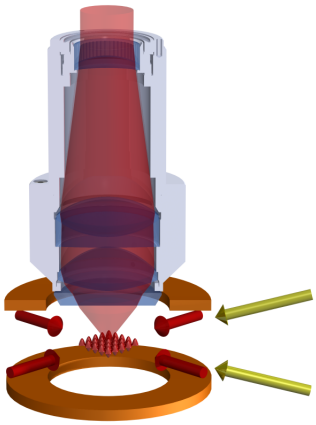

Figure 7.2: Illustration of the optical lattice. The green laser beams create the 2D pancake trap, the red beams the lattice potential. The brown Helmholtz field coils are used to tune the magnetic offset field. We image the two-dimensional system from above using a custom-made high-resolution objective.

After the preparation of a homogeneous two-dimensional Fermi gas in the pancake trap we will overlap this with a two-dimensional optical lattice. For this we will use two retro-reflected 1064 nm laser beams under an angle of 90° which results in a lattice spacing of 532 nm. This is too small to allow for single-site imaging with the high-resolution objective. However, in the future we could also use the objective together with a spatial light modulator to project the lattice potential onto the two-dimensional cloud from above. With this we could increase the lattice spacing to enable single-site imaging or locally adapt the trap depth for lattice cooling schemes. In Figure 7.2 the setup to produce the optical lattice is shown together with the high-resolution objective.
In the two-dimensional optical lattice we will first do some experiments with two-component Fermi gases. A first milestone would be to observe the transition from a superfluid to a fermionic Mott insulator. In the next step we will then study three-component Fermi gases in the two-dimensional lattice system. In this system we are hoping to observe lattice phenomena like loss-blocking due to a quantum Zeno effect and exotic quantum phases like color superfluidity [Kan09].

References

[And95] M. H. Anderson, J. R. Ensher, M. R. Matthews, C. E. Wieman, E. A. Cornell, *Observation of Bose-Einstein condensation in a dilute atomic vapor*, Science **269**(5221), 198–201 (1995).

[Bar57] J. Bardeen, L. N. Cooper, J. R. Schrieffer, *Microscopic theory of superconductivity*, Phys. Rev. **106**(1), 162–164 (April 1957).

[Bar04] M. Bartenstein, A. Altmeyer, S. Riedl, S. Jochim, C. Chin, J. Hecker-Denschlag, R. Grimm, *Crossover from a molecular Bose-Einstein condensate to a degenerate Fermi gas*, Phys. Rev. Lett. **92**, 120401 (March 2004).

[Bra95] C. C. Bradley, C. A. Sackett, J. J. Tollett, R. G. Hulet, *Evidence of Bose-Einstein condensation in an atomic gas with attractive interactions*, Phys. Rev. Lett. **75**, 1687–1690 (August 1995).

[Chi04] C. Chin, R. Grimm, *Thermal equilibrium and efficient evaporation of an ultracold atom-molecule mixture*, Phys. Rev. A **69**, 033612 (March 2004).

[Chi10] C. Chin, R. Grimm, P. Julienne, E. Tiesinga, *Feshbach resonances in ultracold gases*, Rev. Mod. Phys. **82**(2), 1225 (April 2010).

[Dal98] J. Dalibard, *Collisional dynamics of ultracold atomic gases*, in M. Inguscio, S. Stringari, C. Wieman (Ed.), *Bose-Einstein Condensation in Atomic Gases*, Vol. Course CXL of *Proceedings of the International School of Physics Enrico Fermi* (IOS Press, 1998).

[Dav95] K. B. Davis, M. O. Mewes, M. R. Andrews, N. J. van Druten, D. S. Durfee, D. M. Kurn, W. Ketterle, *Bose-Einstein condensation in a gas of sodium atoms*, Phys. Rev. Lett. **75**, 3969–3973 (November 1995).

[DeM99] B. DeMarco, D. S. Jin, *Onset of Fermi degeneracy in a trapped atomic gas*, Science **285**(5434), 1703–1706 (1999).

[Ein25] A. Einstein, *Quantentheorie des einatomigen idealen Gases*, Sitzungsberichte der Preussischen Akademie der Wissenschaften **1**, 3 (1925).

[Ess10] T. Esslinger, *Fermi-Hubbard physics with atoms in an optical lattice*, Annu. Rev. Condens. Matter Phys. **1**, 129–52 (2010).

[Foo07] C. J. Foot, *Atomic physics*, Oxford master series in physics 7: Atomic, optical, and laser physics (Oxford University Press, 2007), 1st Edn.

[Fox06] M. Fox, *Quantum optics : an introduction* (Oxford University Press, 2006).

[Geh03] M. E. Gehm, *Properties of ^{6}Lithium* (2003).

[Gio96] S. Giorgini, L. P. Pitaevskii, S. Stringari, *Condensate fraction and critical temperature of a trapped interacting Bose gas*, Phys. Rev. A **54**, R4633–R4636 (December 1996).

[Gio08] S. Giorgini, L. P. Pitaevskii, S. Stringari, *Theory of ultracold atomic Fermi gases*, Rev. Mod. Phys. **80**(4), 1215–1274 (October 2008).

[Gre03] M. Greiner, C. A. Regal, D. S. Jin, *Emergence of a molecular Bose-Einstein condensate from a Fermi gas*, Nature **426**, 537–540 (2003).

[Gri00] R. Grimm, M. Weidemüller, Y. B. Ovchinnikov, *Optical dipole traps for neutral atoms*, Adv. At. Mol. Opt. Phys. **Vol. 42**, 95–170 (2000).

[Heu11] S. Heupts, *A new radio frequency setup to manipulate spin mixtures of fermionic atoms*, Bachelor thesis (September 2011).

[Hof02] W. Hofstetter, J. I. Cirac, P. Zoller, E. Demler, M. D. Lukin, *High-Temperature superfluidity of fermionic atoms in optical lattices*, Phys. Rev. Lett. **89**, 220407 (November 2002).

[Ino98] S. Inouye, M. R. Andrews, J. Stenger, H.-J. Miesner, D. M. Stamper-Kurn, W. Ketterle, *Observation of Feshbach resonances in a Bose-Einstein condensate*, Nature **392**, 151–154 (March 1998).

[Joc03] S. Jochim, M. Bartenstein, A. Altmeyer, G. Hendl, S. Riedl, C. Chin, J. Hecker-Denschlag, R. Grimm, *Bose-Einstein condensation of molecules*, Science **302**(5653), 2101–2103 (2003).

[Kan09] A. Kantian, M. Dalmonte, S. Diehl, W. Hofstetter, P. Zoller, A. J. Daley, *Atomic color superfluid via three-body loss*, Phys. Rev. Lett. **103**, 240401 (Dec 2009).

[Ket99] W. Ketterle, D. S. Durfee, D. M. Stamper Kurn, *Making, probing and understanding Bose-Einstein condensates*, in M. Inguscio, S. Stringari, C. Wieman (Ed.), *Bose-Einstein Condensation in Atomic Gases*, Vol. CXL of *Proceedings of the International School of Physics Enrico Fermi*, 67–176 (IOS Press, 1999).

[Ket08] W. Ketterle, M. W. Zwierlein, *Making, probing and understanding ultracold Fermi gases* (2008).

[Lin93] J. L. Lin, J. P. Wolfe, *Bose-Einstein condensation of paraexcitons in stressed* Cu_2O, Phys. Rev. Lett. **71**, 1222–1225 (August 1993).

[Lom08] T. Lompe, *An appartus for the production of molecular Bose-Einstein condensates*, Diploma thesis (2008).

[Lom10] T. Lompe, T. B. Ottenstein, F. Serwane, A. N. Wenz, G. Zürn, S. Jochim, *Radio-frequency association of Efimov trimers*, Science **330**(6006), 940–944 (2010).

[Luo06] L. Luo, B. Clancy, J. Joseph, J. Kinast, A. Turlapov, J. E. Thomas, *Evaporative cooling of unitary Fermi gas mixtures in optical traps*, New Journal of Physics **8**(9), 213 (2006).

[Met02] H. J. Metcalf, P. v. Straten, *Laser cooling and trapping*, Graduate texts in contemporary physics (Springer, 2002), corr. 2. print Edn.

[O'H02] K. M. O'Hara, S. L. Hemmer, M. E. Gehm, S. R. Granade, J. E. Thomas, *Observation of a strongly interacting degenerate Fermi gas of atoms*, Science **298**, 2179–2182 (2002).

[Ott08] T. B. Ottenstein, T. Lompe, M. Kohnen, A. N. Wenz, S. Jochim, *Collisional stability of a three-component degenerate Fermi gas*, Phys. Rev. Lett. **101**, 203202 (November 2008).

[Pet02] C. J. Pethick, H. Smith, *Bose-Einstein condensation in dilute gases* (Cambridge University Press, 2002).

[Pet04] D. S. Petrov, C. Salomon, G. V. Shlyapnikov, *Weakly bound dimers of fermionic atoms*, Phys. Rev. Lett. **93**, 090404 (2004).

[Pet05] D. S. Petrov, C. Salomon, G. V. Shlyapnikov, *Scattering properties of weakly bound dimers of fermionic atoms*, Phys. Rev. A **71**, 012708 (2005).

[Pit08] L. P. Pitaevskij, S. Stringari, *Bose-Einstein condensation*, No. 116 in International series of monographs on physics (Clarendon Press, 2008), repr. Edn.

[Rap07] A. Rapp, G. Zaránd, C. Honerkamp, W. Hofstetter, *Color superfluidity and "baryon" formation in ultracold fermions*, Phys. Rev. Lett. **98**, 160405 (April 2007).

[Rie10] M. Ries, *A magneto-optical trap for the preparation of a three-component Fermi gas in an optical lattice*, Diploma thesis (2010).

[Sch05] F. Schwabl, *Quantenmechanik*, Springer-Lehrbuch (Springer, 2005), 6th Edn.

[Ser07] F. Serwane, *The setup of a magneto optical trap for the preparation of a mesoscopic degenerate Fermi gas*, Diploma thesis (2007).

[Ser11] F. Serwane, *Deterministic preparation of a tunable few-fermion system*, Dissertation (2011).

[Sim10] P. Simon, *Apparatus for the preparation of ultracold Fermi gases*, Diploma thesis (2010).

[SK11] D. M. Stamper-Kurn, J. H. Thywissen, *Experimental methods of ultracold atomic physics* (November 2011).

[Smi11] R. P. Smith, R. L. D. Campbell, N. Tammuz, Z. Hadzibabic, *Effects of interactions on the critical temperature of a trapped Bose gas*, Phys. Rev. Lett. **106**, 250403 (June 2011).

[Sta12] J. Stachurska, *An optical dipole trap for two-dimensional confinement of lithium atoms*, Bachelor thesis (2012).

[Tre11] A. Trenkwalder, C. Kohstall, M. Zaccanti, D. Naik, A. I. Sidorov, F. Schreck, R. Grimm, *Hydrodynamic expansion of a strongly interacting Fermi-Fermi mixture*, Phys. Rev. Lett. **106**, 115304 (2011).

[Wac05] A. Wachter, H. Hoeber, *Repetitorium Theoretische Physik*, Springer-Lehrbuch (Springer, 2005), 2nd Edn.

[Wei09] M. Weidemüller, C. Zimmermann, *Cold atoms and molecules* (Wiley-VCH, 2009).

[Wen09] A. N. Wenz, T. Lompe, T. B. Ottenstein, F. Serwane, G. Zürn, S. Jochim, *Universal trimer in a three-component Fermi gas*, Phys. Rev. A **80**, 040702 (Oct 2009).

[Wil07] F. Wilczek, *Quantum chromodynamics: Lifestyles of the small and simple*, Nature Physics **3**, 375–376 (2007).

[Zwi03] M. W. Zwierlein, C. A. Stan, C. H. Schunck, S. M. F. Raupach, S. Gupta, Z. Hadzibabic, W. Ketterle, *Observation of Bose-Einstein condensation of molecules*, Phys. Rev. Lett. **91**, 250401 (Dec 2003).

Danksagung

Mein herzlicher Dank gilt allen, die diese Arbeit ermöglicht haben. Zuallererst möchte ich Selim für die hervorragende Betreuung danken. Vielen Dank dafür, dass Du Dir immer Zeit genommen hast meine Fragen geduldig zu beantworten, dass Du so ein entspanntes Arbeitsklima schaffst und sogar für meine regelmäßigen langen Wochenenden Verständnis hattest.
Bei Matthias Weidemüller bedanke ich mich für die Zweitkorrektur dieser Arbeit.
Mein besonderer Dank gilt der Ultracold-Gruppe: Thomas, Friedhelm, Gerhard, Andre, Martin, Andrea, Sebastian, Juliana und Vincent. Vielen Dank für Eure Unterstützung in allen Belangen. Ihr habt das letzte Jahr unvergesslich gemacht und dafür gesorgt dass ich es nie bereut habe, auf den Berg zu fahren. Im letzten Jahr habe ich gefühlt so viel gelernt wie sonst im ganzen Studium, dazu habt Ihr mit Euren geduldigen und oft wiederholten Erklärungen enorm beigetragen. Auch für mein inzwischen halbwegs passables Kicker-Geschick möchte ich Euch danken, das wird mir sicher auch in den nächsten Jahren sehr zugutekommen. Thomas, Andre und Martin danke ich fürs Korrekturlesen dieser Arbeit. Danke, Andre und Martin, dass Ihr mich so oft mit dem Auto mitgenommen habt und Andre für die morgendliche SMS.
Mein Dank gilt auch den Werkstätten am PI und am MPI, vor allem Herrn Flicker, Herrn Säubert und den Azubis aus der Lehrwerkstatt, ohne die wir die "Schielbrille" nie hingekriegt hätten.
Besonders bedanken möchte ich mich bei Hendrik. Danke, dass Du mir beim Schreiben beigestanden hast, auch wenn ich mal anstrengend war. Und Danke, dass es Dich gibt und Du immer für mich da bist!
Meiner Familie, Jumama, Papa, Joni, Nils und dem großen Seele-Clan, möchte ich für die bedingungslose Unterstützung danken. Ich weiß, dass ich mich immer auf Euch verlassen kann.